JGR Planets

RESEARCH ARTICLE

10.1029/2023JE008123

Amazonian Tectonic Evolution of Ceraunius and Tractus Fossae, Mars, and Implications for Local Magmatic Sources

Stephanie Shahrzad[1], Emma K. Bramham[1], Sandra Piazolo[1], Mark Thomas[1], and Paul K. Byrne[2]

[1]School of Earth and Environment, University of Leeds, Leeds, UK, [2]Department of Earth and Planetary Science, Washington University in St. Louis, St. Louis, MO, USA

Key Points:

- Three fault populations and four types of collapse features are mapped and analyzed in Ceraunius Fossae and Tractus Fossae
- We present a four-stage structural evolution of the area, with dike-induced deformation being the prevalent process
- The stages of activity in the study area all occurred during the Amazonian, with activity from a local magmatic source beneath Ceraunius Fossae

Supporting Information:

Supporting Information may be found in the online version of this article.

Correspondence to:

S. Shahrzad,
eessha@leeds.ac.uk

Citation:

Shahrzad, S., Bramham, E. K., Piazolo, S., Thomas, M., & Byrne, P. K. (2024). Amazonian tectonic evolution of Ceraunius and Tractus Fossae, Mars, and implications for local magmatic sources. *Journal of Geophysical Research: Planets*, *129*, e2023JE008123. https://doi.org/10.1029/2023JE008123

Received 26 SEP 2023
Accepted 14 JUN 2024

Abstract The heavily faulted Martian terrains of Ceraunius Fossae and Tractus Fossae, south of the Alba Mons volcano, have previously only been considered as parts of larger tectonic studies of Alba Mons, and consequently the complexity of the faulting remains unclear. As these terrains are in the midst of the large Tharsis volcanoes, the study of their surface deformation has the potential to help unravel the volcano-tectonic deformation associated with the growth of Tharsis as well as to decipher details of the magma-tectonic processes responsible for graben formation. Here, we distinguish between faults and collapse structures based on image and topographic evidence. We mapped ~12,000 faults, which we grouped into three distinct fault groups based on orientation, morphology, and relative ages. These show a temporal evolution in the mapped fault orientations from NE to N-S to NW with associated changes in stress orientations. We also mapped collapse features and categorized them into four different groups: pit-crater chains, catenae, u-shaped troughs and chasmata. Examining the four collapse structure groups reveals that they are likely four progressive stages in the erosional evolution of pit-crater chains. Together, this revealed a structural history heavily influenced by lateral diking from both local (radial to Alba Mons, Pavonis Mons and Ascraeus Mons) and regional (radial to Tharsis) sources, and vertical diking from a proposed Ceraunius Fossae centered magma source. This, along with an updated crater size-frequency distribution analysis of the unit ages, reveals a highly active tectonic and magmatic environment south of Alba Mons in the Middle Amazonian.

Plain Language Summary The large-scale faults surrounding the dome of the Alba Mons volcano on Mars have been studied intensely, while the faulted area south of Alba Mons has received relatively little attention. Closer inspection of these southern terrains, namely Ceraunius Fossae and Tractus Fossae, reveals that this area is far more complex in structure and more recent in activity than previously thought. In this study, we mapped and measured all the faults in the study areas. In addition to the faults, the surface of the study area is covered in "collapse structures." These are circular to trough-like features created when the surface material has fallen into a subsurface cavity. We mapped and characterized these faults and collapse structures, in order to determine the history of events and which geological process created them. We found three distinct extensional faulting events, and examples of four types of collapse structures. These events all took place within 2.4–1.4 billion years ago during the Amazonian period. Together, these results show that magmatic activity drove structure deformation, both from the surrounding Alba Mons, Ascraeus Mons and Pavonis Mons volcanoes, and also from a local large magmatic source situated directly underneath Ceraunius Fossae.

1. Introduction

With the advent of increasing resolution of Martian image data over the last decades, it has become possible to thoroughly investigate questions related to the tectonic regimes of Mars and determine the influence of various magmatic processes on tectonics. Though larger scale processes on Mars are generally understood, local-scale graben structures observed on Mars remain understudied. Detailed characterization of the surface structures in local areas, and their relationships to large regional or local stress variations and magmatic processes, are essential to understanding the development of the volcanic centers on Mars, and thus the evolution of the planet.

One of these volcanic centers is Alba Mons, a wide low-relief shield volcano located on the northern edge of the Tharsis region (Figure 1). The Alba Mons volcano, and its associated system of extensive graben structures have been studied in detail over the last two decades (e.g., Cailleau et al., 2005; Krishnan & Kumar, 2023; McGovern et al., 2001; Öhman & McGovern, 2014). The fault systems around Alba Mons include Alba Fossae, Tantalus Fossae, Ceraunius Fossae and Tractus Fossae (Figure 1). The different surface expressions of the faults

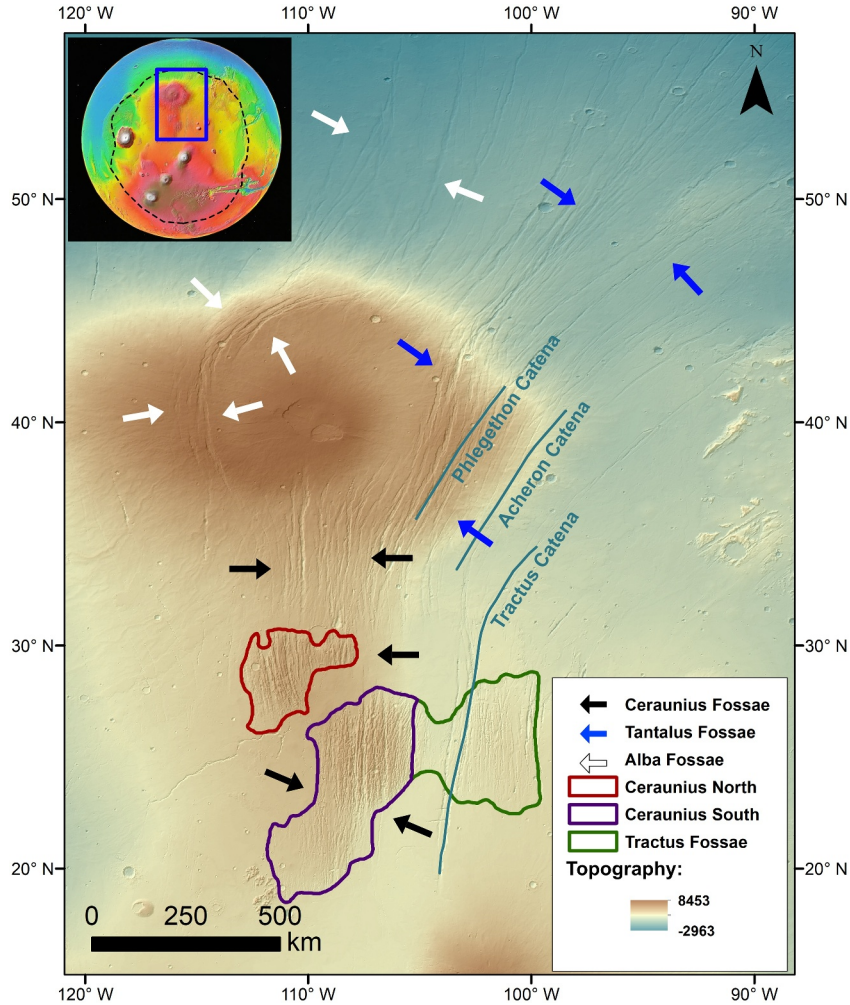

Figure 1. Location of features surrounding the Alba Mons volcano (See context location on top left inset of Mars, with the Tharsis Volcanic Province outlined in black dashed line). The three study areas are outlined in the legend, as mapped by Tanaka et al. (2014). Arrows indicate the extent of three different fossae systems. The three major catenae, Tractus Catena, Acheron Catena, and Phlegethon Catena, are labeled with light blue lines. The background is Mars Orbiter Laser Altimeter (MOLA) Hillshade overlaid by merged MOLA-HRSC (High Resolution Stereo Camera) Digital Elevation model (200 m/px) (Fergason et al., 2018).

surrounding Alba Mons have been mapped to various degrees. However, their interpretations differ significantly and the source of the deformation is still a matter of debate, with interpretations ranging from purely magmatic to purely tectonic processes or a combination of both (Cailleau et al., 2003; Ivanov & Head, 2006; Stubblefield, 2018; Öhman & McGovern, 2014).

The Tharsis volcanic province is the largest volcano-tectonic center on Mars and hosts hundreds of volcanic edifices and their associated tectonic deformation (Pieterek et al., 2022; Plescia & Saunders, 1982) as well as thousands of identified small volcanic vents (Richardson et al., 2021). In the study area south of Alba Mons, 20 dated landforms reveal that the ages of the latest volcanic activity range between 421 and 68 Ma (Pieterek et al., 2022). The region of Tharsis has been in continuous development since >3.7 Ga (e.g., Plescia, 1994; Werner, 2009), with volcanic activity measured as recently as 200 Ma ago during the Amazonian (e.g., Hauber et al., 2011; Pieterek et al., 2022). The source of the extensive volcanism in the Tharsis province has been attributed to the activity of the Tharsis superplume (e.g., Dohm et al., 2007; Mège & Masson, 1996). The superplume, consisting of several mantle plumes, is thought to have been emplaced underneath the entire volcanic province. The superplume was acting as the driving factor in the construction of Tharsis from the Noachian through to the Amazonian. However, recent research has suggested that the magma source beneath Alba Mons,

which would be responsible for the low-angle slope of the volcano and the extensive surface deformation surrounding it, is a separate, possibly independent plume from the Tharsis superplume (Belleguic et al., 2005; Cailleau et al., 2005; Öhman & McGovern, 2014). This theory has its origins in the gravity study of Tharsis by Janle and Erkul (1991), who concluded that a separate diapir is responsible for Alba Mons.

The majority of the Alba Mons studies focus on the extensive structures immediately surrounding the edifice (e.g., Cailleau et al., 2005; Ivanov & Head, 2006; McGovern et al., 2001). The notable exceptions to this are the extension and mechanical stratigraphy studies by Borraccini et al. (2005, 2006), and the recent study by Krishnan and Kumar (2023), where selected lava flows, grabens, volcanic pits and boulders were analyzed to construct a geodynamic setting. The faults of Tractus Fossae have been the focus of one previous study (Spagnuolo et al., 2008), though the area is not considered in relation with the neighboring Ceraunius Fossae. Despite these analyses, detailed fault mapping of the area south of Alba Mons is still needed in order to establish a structural history of the area.

In this study, we present a novel combination of comprehensive mapping, morphological analysis, and strain calculation for the faults in the area south of Alba Mons, along with updated absolute model ages for the associated geological units. Additionally, we mapped and categorized the observed collapse structures and determined any connections to the mapped faults in order to determine the conditions that would cause the collapse features to form, as well as any progression in structure. We used these analyses as the basis for determining the likely sources of both faults and non-fault structures and produced a sequence of structural events. By coupling this sequence of events with the large- and small scale tectonic and magmatic influences responsible for shaping the current surface around Alba Mons, we were able to further illuminate the magmatic and tectonic history of the Tharsis volcanic province, and Mars as a whole.

1.1. Geological Setting

1.1.1. Morphological Characteristics of the Alba Mons Volcano

Alba Mons, previously referred to as "Alba Patera" has a diameter of ∼1,600 km, a ∼7 km relief and a ∼1° flank slope angle, making it the largest edifice of any volcano on Mars (Plescia, 2004). The northern flank of Alba Mons is located proximal to the Martian dichotomy boundary, along the margin between the southern highlands and the northern lowlands (Ivanov & Head, 2006). The summit of the volcano is host to a complex of calderas which have been dated between $3.02^{+0.32}_{-0.9}$ Ga and 450 ± 100 Ma (Robbins et al., 2011), extensive lava flows along its flanks, and one of the largest graben complexes on Mars (Ivanov & Head, 2006). The edifice itself is surrounded by Amazonian lava flows, with some topographically raised patches of older Hesperian material to the south at Ceraunius Fossae and Tractus Fossae (Tanaka et al., 2014). It was later suggested in a study by Pieterek et al. (2022) that the age of Ceraunius Fossae should be revisited as it is host to Amazonian-age volcanic edifices.

1.1.2. Graben Structures Associated With Alba Mons

Alba Mons is surrounded by complex graben systems, which are categorized into four geographical groups (Figure 1): Tantalus Fossae (E and NE of Alba Mons), Alba Fossae (W and N of Alba Mons), Ceraunius Fossae (S of Alba Mons), and Tractus Fossae (SE of Alba Mons). The graben can also be divided based on morphology into the following groups: (a) north and northeast trending linear grabens and (b) concentric grabens that form the circumferential structures around the Alba Mons volcanic dome (Cailleau et al., 2003). Tantalus Fossae are linear grabens bounding Alba Mons with an average strike orientation of N/NE (blue arrows on Figure 1) and are considered the oldest of the graben systems. They are assumed to have been formed by a combination of regional stress and a broad uplift due to a buoyancy zone underneath Alba Mons. This was reproduced in modeling studies by Cailleau et al. (2003) and Polit et al. (2009).

Following the formation of these linear grabens, there was a change in the development of the circumferential (concentric) grabens of Alba Fossae, which are prevalent on the western flank of the Alba Mons volcano (white arrows on Figure 1). Increasing subsidence, associated with the formation of Alba Mons, created a regime with a predominance of concentric faults in later stages of faulting (Polit et al., 2009), superimposing the subsidence related graben formation on the effects of regional extension. This was also reproduced in numerical and physical models by Cailleau et al. (2003).

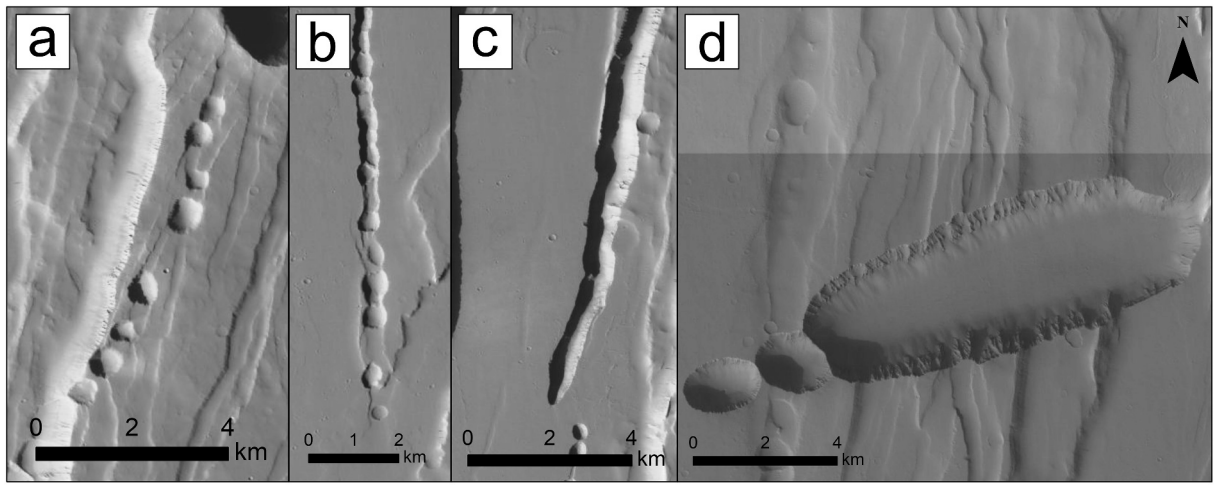

Figure 2. Zoom of example of variety of collapse structures found in the study areas. (a) Example of pit-crater chain, feature centered at 29°39′15.17″N, 108°22′43.83″W. (b) Example of catenae, feature centered at 26°55′38.14″N, 109°2′48.46″W. (c) Example of a u-shaped trough, feature centered at 29°28′19.54″N, 108°28′12.44″W. (d) Example of a chasma, feature centered at 19°56′3.73″N, 108°55′0.71″W. CTX background Global Mosaic credit: Esri, Caltech Murray Lab, NASA, JPL, MSSS.

1.1.3. Collapse Features

In addition to the faults, the southern Alba Mons area has a series of distinct, non-fault surface features which vary significantly in morphology, location, and size, and are similar to other Martian terrains affected by volcanism (Figure 2). These features include pit-crater chains, catenae, u-shaped troughs and chasmata, which we collectively refer to as "Collapse Features." Definitions of these feature types have been described in previous literature on Mars (e.g., Hardy, 2021; Mège et al., 2002, 2003). Pit-crater chains (PCCs) are made of craters formed by the collapse of material into subsurface voids, rather than by impacts. Such voids can be the result of various processes, but the most widely accepted ones are tension fractures, collapse of lava tubes, dike-generated volatile release, or magma withdrawal (Cushing et al., 2015; Ferrill et al., 2011; Wyrick et al., 2004). The orientation of the chain reflects the collapsed structure underneath (Mège et al., 2002). Catenae is the term for a chain of pit-craters where the craters interact with each other either due to the initial close proximity of craters during formation or due to further erosion of a "standard" pit-crater chain where the isolated craters are enhanced and thus interact. U-shaped troughs are elongated troughs, which can vary drastically in orientation along the strike and terminate in a circular shape, connecting the two sides of the trough (Mège et al., 2003) (Figure 2c). Finally, the chasmata are generally observed as large erosional features (Figure 2d), possibly induced by initial pit-crater chains as well, or perhaps from collapse into larger cavities than u-shaped troughs (Mège et al., 2003). Despite this qualitative understanding, it remains unclear exactly how these four collapse features are related to each other, and how they are related to the complex magma-tectonic environment on Mars.

1.1.4. Expected Observations for Faulting Driven by Intrusions or Pure Tectonic Deformation

Grabens formed by dike intrusion initiated faulting, commonly have a uniform width, depth, and length (Tanaka et al., 1991). These grabens are generally narrow and symmetrical (Mège, 1999) with a radial or fan-shaped fault population geometry extending from a volcanic source (Carr, 1974; Mège & Masson, 1996). They are also often associated with other linear surface features such as pit-crater chains, chasmata and u-shaped troughs (Mège & Masson, 1996). For purely tectonic extensional faulting, we expect fewer narrow grabens with less symmetrical and more irregular spatial fault patterns within a population. In terms of geometry, grabens associated with volcanic loading, uplift, or subsidence will show circumferential, wristwatch, or hourglass patterns (Byrne et al., 2015; Cailleau et al., 2003, 2005). Non-volcanic tectonism such as flexural loading, uplift, or isostatic compensation will generally be accompanied by either radial or circumferential wrinkle ridges (i.e., compression) (Banerdt et al., 1992; Tanaka et al., 1991).

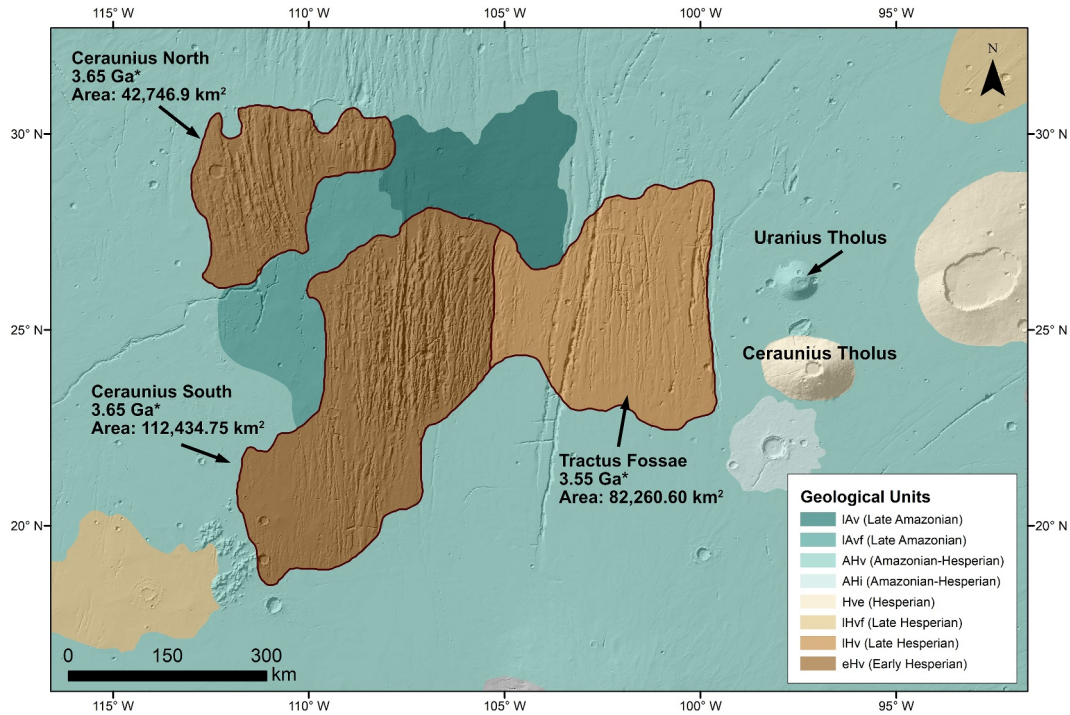

Figure 3. Geologic map of the three study areas with unit outlines as defined by Tanaka et al. (2014). Note the names Ceraunius North (unit eHv), Ceraunius South (unit eHv) and Tractus Fossae (unit lHv) used to identify each unit in this study, and the area measurement for each study area. *The Tanaka et al. (2014) mapped unit age. Background image is MOLA hillshade.

1.2. Study Areas: Selection, General Characteristics, and Previous Studies

1.2.1. Selection of Study Areas

We selected two fossae systems, Ceraunius Fossae and Tractus Fossae, across three geological units south of Alba Mons as our study areas for this work (Figure 3). While Ceraunius Fossae continues further north onto the flank of Alba Mons (Figure 1), we focus solely on the southern sections of Ceraunius Fossae, as defined within the Tanaka et al. (2014) mapped geological unit boundaries (Figure 3). Though the western border of Tractus Fossae is commonly defined by Tractus Catena, we investigated all features within the mapped l Hv unit (Figure 3). Tanaka et al. (2014) previously mapped these three areas as separate geological units, allowing for more dependable ages constrained using the crater size-frequency distribution method. As the south of Ceraunius Fossae is divided into two units with a young lava flow separating the two areas (Figure 3), we refer to these regions and their faults as Ceraunius North and Ceraunius South. Ceraunius and Tractus fossae serve as examples of linear and curved faulting potentially related to Alba Mons, and possibly host a transition between the two types of faulting. At initial inspection the two areas also include a number of non-graben features with potential magmatic or volcanic origin, which we identify as the collapse features (Mège et al., 2003). Additionally, these study areas have a similar distance from their nearest volcanic edifice (of ~600 km from Alba Mons) as Ulysses Fossae (~600 km from Olympus Mons) as described by Shahrzad et al. (2023), which allows us to compare results and ultimately broaden our understanding of the Tharsis volcanic region.

1.3. General Characteristics and Previous Studies

1.3.1. Ceraunius Fossae North and South

The faulted terrain immediately to the south of the Alba Mons shield is a part of the *Ceraunius Fossae* system (Figure 1). It consists of a dense array of linear faults that appear to be oriented generally north-south, largely radial to the Alba Mons shield. The extent of our mapping of the Ceraunius Fossae fault system is contained in two raised patches of early Hesperian volcanic unit (eHv) with an absolute age of 3.65 Ga (Tanaka et al., 2014)

covered by extensive faults and grabens (Figure 3). These elevated patches are separated by lower-elevation, younger lava flows, effectively preserving a significantly larger number of structural features than those of the surrounding flooded plains. Previous work by Tanaka (1990) determined a two-stage sequence of faulting in the area, with an initial NE and then N-S oriented extensional events.

1.3.2. Tractus Fossae

The Tractus Fossae region is located immediately to the east of Ceraunius Fossae, and constitutes a unit mapped by Tanaka et al. (2014) as l Hv, the late Hesperian volcanic unit. This unit is aged 3.55 Ga (Tanaka et al., 2014), and is thus considered the youngest of the three study areas. Immediately to the east of the area, the two volcanoes Uranius Tholus and Ceraunius Tholus are located, with diameters of ∼60 and ∼130 km, respectively (Figure 1). Tractus Fossae is intensely faulted with large linear grabens, though they appear more spread out than those in Ceraunius Fossae. Tractus Fossae is also host to two large linear structures along its western border that are longer and deeper than the other grabens in the area, with Tractus Catena being the only one. This area has only one dedicated study, by Spagnuolo et al. (2008), which identified the faulting in Tractus Fossae as early as the Noachian-Hesperian boundary, followed by some faulting in the Amazonian.

2. Methods

2.1. Fault Characterization

2.1.1. Fault Mapping and Grouping

We mapped the faults in this study using 6 m/pixel resolution global image mosaic from the Mars Reconnaissance Orbiter's Context Camera (CTX) (Image credit: Esri, Caltech Murray Lab, NASA, JPL, MSSS). We mapped the fault traces as separate polylines using Esri ArcMap software (v. 10.6), at a scale of 1:250,000–1:10,000, where we traced the upper boundary of the fault (surface breaks). For our three study areas of Ceraunius North, Ceraunius South and Tractus Fossae, we used the Tanaka et al. (2014) geologic map as unit boundaries and mapped the faults within. Any fault that started within the defined study area boundary was mapped in full even if the trace continued beyond the boundary. We aimed to map all identifiable faults at the chosen scale, in order to capture each fault trend. For fault length determinations, we only considered any fault linkage visible on the surface (hard-linked faults), and we have not made any conjectures regarding supposed sub-surface linkage of potentially soft-linked faults. We calculated the absolute lengths and strike orientations as geodesic lengths and azimuths using the Tools for Graphics and Shapes plugin for ArcGIS (Jenness, 2011). We also used the software package FracPaQ (Healy et al., 2017) to visualize fault strikes spatially and in rose diagrams, along with the mapped fault intensity. In FracPaQ, fault intensity (m^{-1}) is determined by the number of faults intersecting the perimeter of a program generated scan circle (Healy et al., 2017). We used a grid comprised of scan circles with a diameter of ∼10 km, to ensure that the maps captured the complexity of the faulting in the area. Following fault mapping, we separated the mapped faults into different groups defined by similar average orientations, fault morphologies, and the relative ages determined by their crosscutting relationships. This ensured that the faults within a group are all of similar ages and are therefore inferred to have formed through the same structural event.

2.1.2. Strain Measurements for Faults

We measured the strain for each defined fault group using sets of topographic profiles created perpendicular to the main fault orientation in each group. For topography, we used the global Digital Elevation Model (DEM) from the coupled Mars Orbiter Laser Altimeter (MOLA) and the High-Resolution Stereo Camera (HRSC) data (Fergason et al., 2018). The coupled MOLA-HRSC DEM data have a vertical resolution of 1 m/px and a horizontal resolution of 200 m/pixel (Fergason et al., 2018). In QGIS software, we set the location of each topographic profile so it was perpendicular to the average fault orientation within a group and so the trace would not cross any other major topographic features, such as craters, while still capturing as many faults as possible. This process was somewhat limited by the quality of the DEM data in certain areas with regard to resolving individual features.

We measured the extensional strain (ϵ) by calculating the sum of measured throws (Shahrzad et al., 2023) and used a 60° fault dip (consistent with previous Martian estimations (Polit et al., 2009)), to calculate the cumulated extension (e_{cum}). The cumulated extension was then divided by the original length of the profile trace (L_0), defined as the trace length minus the sum of the heaves, to give strain.

$$\epsilon = \frac{e_{\text{cum}}}{L_0}$$

We then multiplied the result by 100 to obtain the strain percent value.

2.2. Collapse Feature Mapping

The collapse features in the three study areas were similarly mapped by marking each feature with a polyline in ArcMap, which went through the middle of the feature and recorded their location and orientation. The four collapse features were identified during the mapping as follows:

Pit crater chains and catenae (see Figures 2a and 2b for examples) were the simplest to identify, as the craters make them non-ambiguous. These features are straightforward to identify on the CTX images alone, where the distinction from individual pit craters to catenae is determined by when the craters touch or directly interact with each other, while the individual craters are still identifiable. *U-shaped troughs* were more difficult to distinguish from the tectonic grabens as they have largely similar straight linear borders. However, they vary from the grabens by several features: (a) uneven border walls with some indications of remnant circular crater perimeter features (scalloped edges). (b) Contrary to the tectonic faults which remain parallel through their trace, the troughs terminate in a semi-circular shape where the walls connect (Figure 2c). As the u-shaped troughs can be a challenge to distinguish, the mapping of them is aided by comparing the CTX images with the MOLA-HRSC topographic data. As we determine u-shaped troughs as a stage in the evolution of the pit-crater chains, the majority of the troughs reveal distinct pit crater chains beneath them on the topographic data, distinguishing them from the purely tectonic faults. The final collapse feature, *chasmata*, can appear similar to u-shaped troughs but is larger in size and commonly forms large oval structures (Figure 2d) (Mège et al., 2003). They are often bounded by faults, with interiors that show evidence of large-scale mass wasting, slopes of material along the sides, and lacking flat graben floors, distinguishing them from the defined slope breaks of the purely tectonic faults. See Figure S1 in Supporting Information S1 for examples of topographic profiles. After mapping each feature, we measured the orientation and length of the features using the Tools for Graphics and Shapes plugin in ArcMap.

2.3. Determining Relative and Absolute Ages

We determined the timing of the activity of the different defined fault groups as constrained by their absolute maximum ages and their relative ages. The maximum absolute ages were determined by the age of the geological unit the fault groups crosscut, which we determined in this study using crater size-frequency distributions. The vast majority of the fault groups in this study crosscut multiple geological units, and in these cases, we assigned the youngest unit age as the maximum age for the group. For the relative ages of the fault groups themselves, we used their crosscutting relationships.

2.3.1. Crater Size-Frequency Distribution

We obtained absolute model ages for the geological units of the three study areas (Figure 3) using the crater size-frequency distribution (CSFD) method in a similar approach to Shahrzad et al. (2023). We mapped all identifiable craters which had a diameter >800 m, with the aim of using all mapped craters ≥1 km in the age determination. This mapping of smaller diameters than the aim ensured that no craters ≥1 km were missed. The crater sizes and locations were mapped in ArcMap using the CraterTools plugin (Kneissl et al., 2011). During mapping, we ensured no capturing of secondary craters (clustering) or other circular features that may have been mistaken for a primary impact crater, such as pit-crater chains. We used the software Craterstats v.2 (Michael, 2013) to fit our crater data to the Martian isochrons, using the production function of Hartmann (2005) and the chronology function of Hartmann and Daubar (2016). We then fit counted craters with a lower diameter boundary of 1 km. Using Craterstats software, we also performed a randomness analysis on the craters in order to verify that secondary craters were not used to fit to the isochron. We make use of both the randomness analyses available in Craterstats. First, the Standard Deviation of Adjacent Area (SDAA) method and the Mean 2nd-Closest Neighbor Distance (M2CND) method. The SDAA method constructs polygons, where the distance of any point to the associated crater centroid is less or the same as to the centroid for any other crater. The SDAA value is then the standard deviation of the area of all polygons (Riedel et al., 2021). The M2CND method determines the distance to the second closest crater centroid for each crater centroid, with the mean of these values used as the M2CND

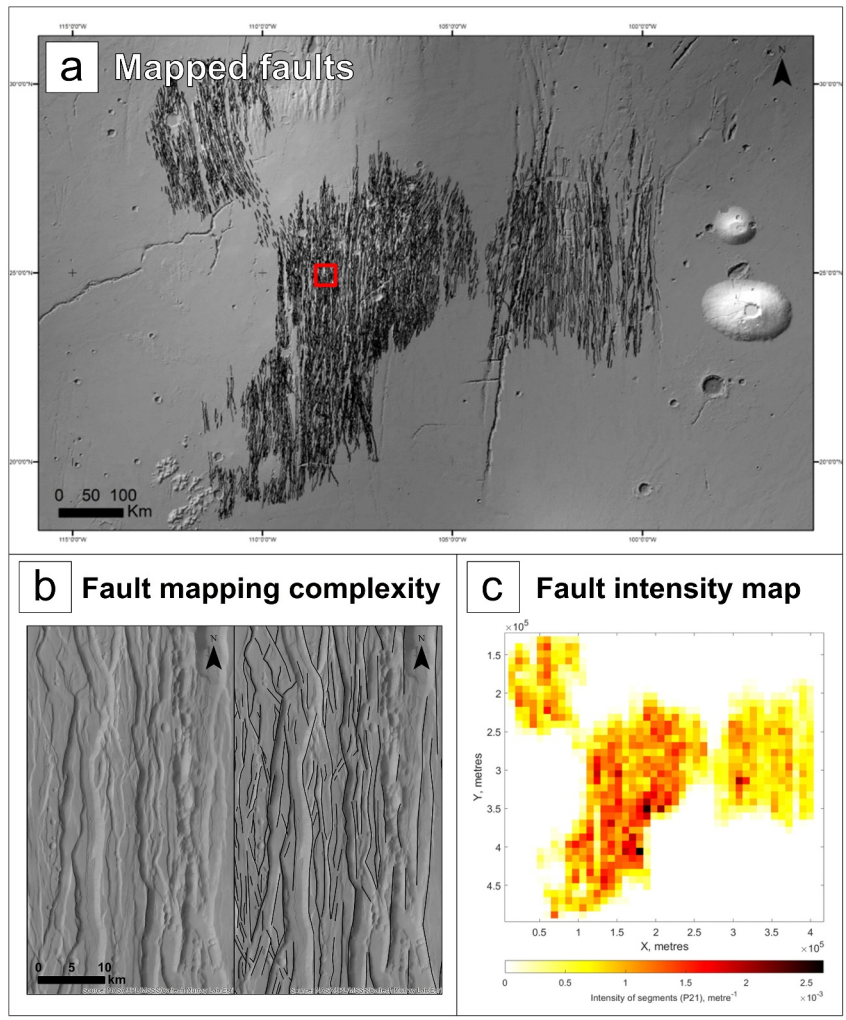

Figure 4. (a) All mapped faults (black lines) in the study area. Red square note's location for zoom in (b) The background is MOLA Hillshade overlaid by merged MOLA-HRSC DEM (200 m/px) (Fergason et al., 2018). (b) Zoom on example of overprinted fault patterns. Left image is area before mapping, right image is area after mapping; black lines show the identified faults. Background Image credit: Esri, Caltech Murray Lab, NASA, JPL, MSSS. (c) FracPaQ generated fault intensity map of mapped faults.

(Riedel et al., 2021). The Craterstats software produces an n_σ diagram showing the degree of clustered or ordered craters in the data set. In this plot, values within the gray shaded area ($\pm 3\sigma$) are not considered clustered or ordered, and therefore show data of good quality with no secondary craters captured with reliable results.

3. Results

3.1. Fault Mapping

We mapped a total of ~12,000 faults in the south of Alba Mons (Figure 4a), across the three study area units, the vast majority of which are graben-forming normal faults which have an average strike orientation between NNW and NNE. The faults heavily overprint each other (Figure 4b) and have a largely similar appearance and morphology. The majority of the grabens are linear, but there are a number of faults with variations in orientation along the strike, with some of them being subtly curved, for example, the eastern faults in Ceraunius North (Figure 4a). We have mapped a cumulative fault length of 106,516.6 km, with the average fault length being ~8 km (see Figure S2 in Supporting Information S1 for histogram of all mapped fault lengths). Among the three geological units, the fault intensity map revealed a relatively even spatial distribution between the two flanking units Ceraunius North and Tractus Fossae, with the middle Ceraunius South unit having the highest intensity of

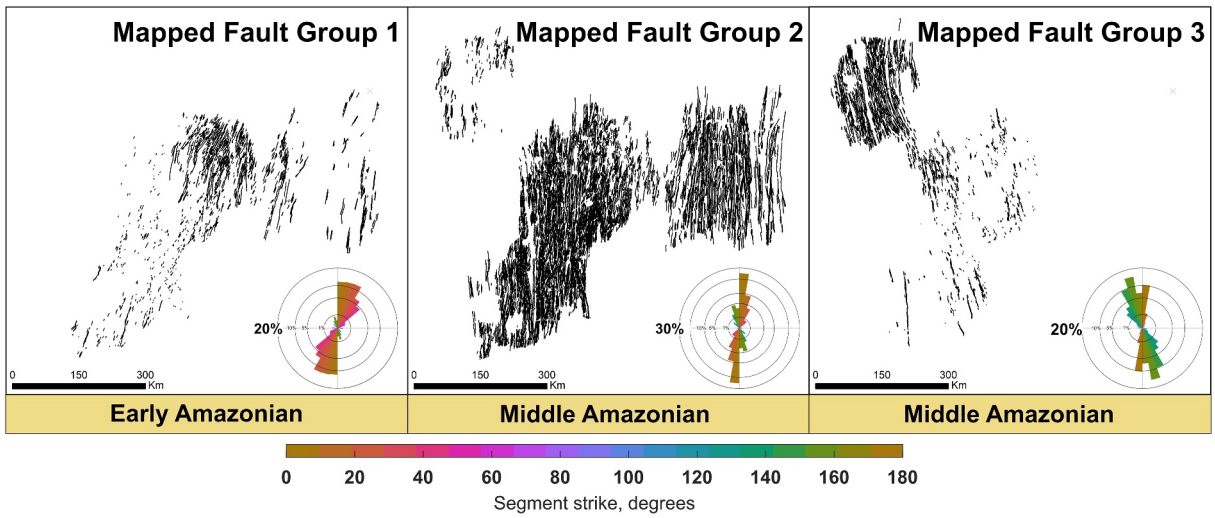

Figure 5. The three fault groups identified in Ceraunius Fossae and Tractus Fossae, with main fault orientations shown in the FracPaQ generated rose-diagrams. See Figure S3 in Supporting Information S1 for rose diagrams for each fault group separated into each study area.

faulting (Figure 4c). Common for all the grabens mapped is the consistent width across strike, which is constantly a few km (2–4 km), resulting in relatively narrow grabens when considering their lengths.

3.1.1. Fault Groups

The initial approach of dividing the faults into groups based on cross-cutting relationships alone proved difficult due to the highly overprinted nature of the faulting (Figure 4b). This was particularly true for the N-S oriented faults in Ceraunius South, where it was challenging to distinguish if faults were changing orientation along strike within a group or if a fault should belong to an entirely different group with a different average orientation. To allow a more detailed and consistent identification of fault groups, we expanded on our initial method. We used the general N-S orientation of the majority of the faults as the baseline for the first group, and then systematically marked any individual fault which (a) had a discernibly different average strike orientation from the N-S group (see rose diagrams in Figure 5) and which (b) crossed the N-S fault independently and was clearly not a branch from the N-S fault orientation group. This left us with two initial fault groups, the N-S group, and a second group of faults that did not belong to the N-S group. We then analyzed the second group and used our original criteria of clear cross-cutting relationships and different strike orientations to further divide that group into two groups, conclusively resulting in three final fault groups in our study area (Table 1). See Figure 5 for the groups.

Group 1 is a relatively sparse group of faults, which crosscut the Tractus Fossae and Ceraunius South units. The main strike orientation is toward NNE, with some subtly curved faults within the Ceraunius South section of faults, which start with a NNE orientation, and then curves more toward the NE, the further north the trace goes. The faults in Group 1 have very few interactions with the Group 3 faults; therefore, we use the Group 2 faults to determine relative ages. The orientations of faults in Group 1 overlapped with the faults in Group 2 and were therefore distinguished from each other using cross-cutting relationships. In places where the two groups interact, the faults in Group 1 are consistently crosscut by the faults in Group 2, making the Group 1 faults the oldest of the two groups.

Table 1
Overview of the Three Fault Groups

Fault group	(N) Faults	Cumulative length (KM)	Avg. Orientation	Unit
G1	1,676	13,061	NNE/NE	CS, TF
G2	8,013	76,213	N/NNE	CN, CS, TF
G3	2,242	17,241	NNW/NW	CN, CS

Note. Which units the faults in the group superpose: CN (Ceraunius North), CS (Ceraunius South), TF (Tractus Fossae).

Table 2
Overview of the Results of Crater Size-Frequency Distribution Model Ages for the Three Geological Units in This Study: Ceraunius North, Ceraunius South, and Tractus Fossae

Area name	Unit name[a]	(N) Craters >1 KM	Unit age	Period
CERAUNIUS NORTH	Early Hesperian volcanic unit (eHv)	34	1.4 ± 0.2 Ga	Middle Amazonian
CERAUNIUS SOUTH	Early Hesperian volcanic unit (eHv)	143	2.2 ± 0.2 Ga	Early Amazonian
TRACTUS	Late Hesperian volcanic unit (lHv)	115	2.4 ± 0.2 Ga	Early Amazonian

[a]Unit name is according to the Tanaka et al. (2014) mapping.

Group 2 consists of faults with a largely N-S orientation, and the majority of them (the Ceraunius South faults) are radial to the main Alba Mons edifice. It is by far the most populous group, containing ∼70% of all the mapped faults. The faults in this group are mostly linear but due to heavy overprinting the faults appear to braid or branch in between each other (Figure 4b). The faults are largely contained within the unit boundaries, but Group 2 is the only group with faults which crosscut all three study areas and thus interacts with the two other fault groups.

The faults in Group 3 appear to crosscut the faults in Group 2 and are therefore the youngest of the three groups. These faults appear only on Ceraunius North and Ceraunius South and have almost no interactions with Group 1. However, similar to Group 1, a portion of faults in this group are also curved, though their orientation is mirrored from Group 1. In Group 3, the curved faults, which are located in the eastern part of Ceraunius North, curve from a NW to NNW orientation the more north the fault trace appears. The linear faults in the south and west maintain an NNW orientation through the strike. The faults in Group 3 also show two very wide graben features, where the largest normal fault-bounding graben is ∼10 km in width.

3.2. Strain

We measured the strain across all three defined fault groups, and determined maximum strains of 2%, 3.2%, and 2.3% for Groups 1, 2, and 3, respectively. As both Groups 1 and 3 had a comparable number of faults (Table 1), with the faults spread over a similar area, the resemblance in strain % was not surprising. The strains for Group 2 are the highest, corresponding to the largest number of faults.

3.3. Absolute Ages

We determined the ages of the three units in Ceraunius Fossae and Tractus Fossae using CSFD and plotted the ages in Craterstats v.2. The crater data were constrained using a 4th root-2 binning, and a Poisson distribution fit (Michael et al., 2016). These mapped craters resulted in three best-fit Amazonian model absolute ages for the units, with Ceraunius North exhibiting a ∼1 Ga younger age than the other two units (Table 2). The CSFD plots and associated n_σ plot for each of the three study areas are shown in Figure 6. Generally, there is an acceptable fit of crater data to the isochrons, with some of the larger crater bins slightly separating from the isochron fit for Ceraunius North and South, but as they are still within their error bars, we consider these ages in the discussion section. The randomness analysis using the SDAA and the M2CND techniques both fall within the $\pm 3\sigma$ area, and we therefore do not consider any of the crater data used to determine these absolute model ages to be too clustered or ordered to fit to the isochrons.

These results all suggest a maximum age for the mapped faulting in our study areas to be Amazonian, with the oldest material being Early Amazonian. This is the case for the faults in Group 1 (Figure 5), which crosscut both Ceraunius South and Tractus Fossae but not Ceraunius North. Due to the group being crosscut by Group 2, which is then crosscut by Group 3, we determine the Group 1 faults as the oldest of the mapped faults. Group 1 is then chronologically followed by Group 2 and then Group 3, where both groups crosscut the youngest unit, Ceraunius North, which has a Middle Amazonian age of 1.4 Ga (Table 2). For groups 1 and 3, the southern section of faults is highly fragmented, and shorter than the northern faults of similar orientation. We attribute this to the high degree of overprinting of faults, where the high intensity faulting (Figure 4b) is obscuring the actual fault traces of any not N-S oriented faults.

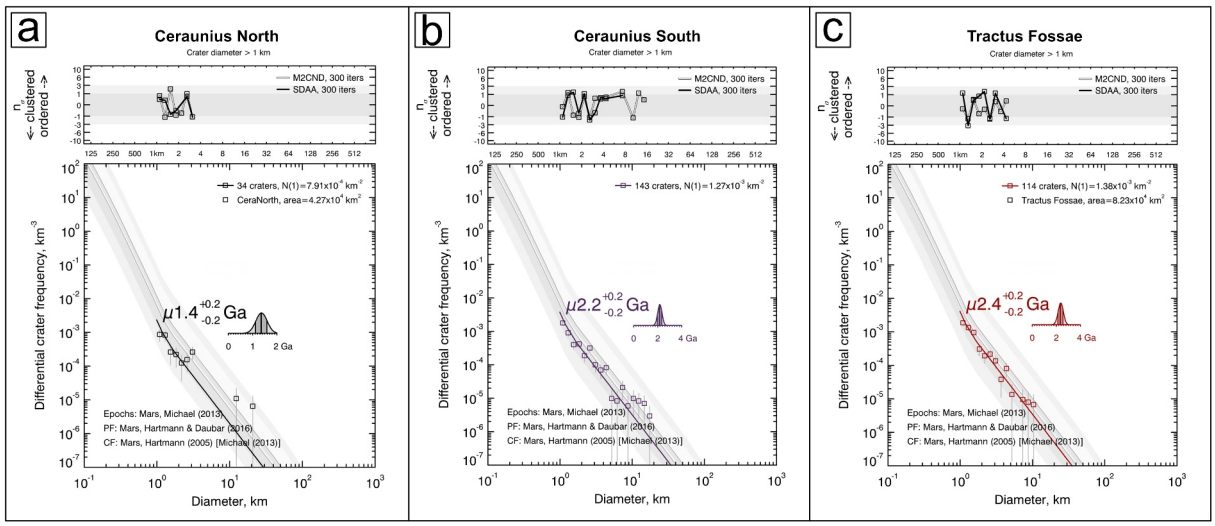

Figure 6. Crater Size-Frequency distribution (CSFD) plots produced in Craterstats v. 2 for (a) Ceraunius North, (b) Ceraunius South and (c) Tractus Fossae. Note the n_σ plot above each isochron plot, presenting the results of the two Craterstats' randomness analysis methods.

3.4. Collapse Structures

During our mapping, we came across four distinct types of collapse features, as described in the methods section. These were mapped separately, and we present an overview of the structures in Figure 7: The spatial distribution of mapped collapse features varies slightly across the three study areas, with Ceraunius North hosting 23.4% of the total collapse structures, 49.9% in Ceraunius South, and 26.7% in Tractus Fossae. Tractus Fossae is also host to the longest collapse structures, with average lengths of ∼16 km, and the longest feature, a u-shaped trough, measuring 146 km long.

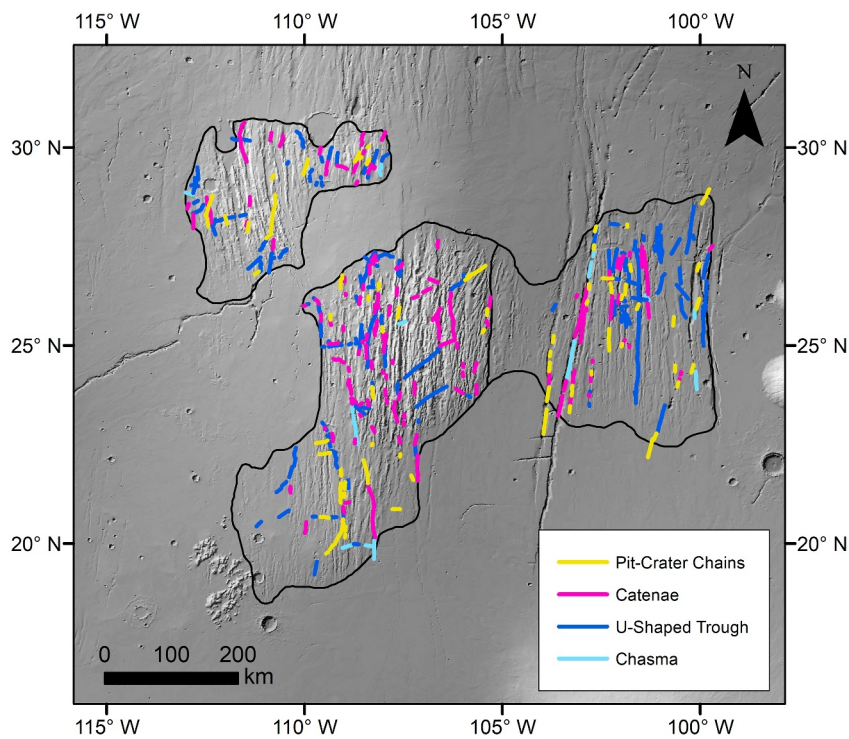

Figure 7. Location of mapped collapse features in the three study areas. Features are color coded by type as shown in the legend. The background is MOLA Hillshade overlaid by merged MOLA-HRSC DEM (200 m/px) (Fergason et al., 2018).

Table 3
Overview of Mapped Collapse Features Separated Into the Four Different Types

Feature name	Number of features	Prevalent Orientations	Cumulative length (km)	Average length (km)	Characteristics
Pit-Crater Chains	81	N-S/NNE	895.3	11.1	• Separate craters in chain. • Majority located within grabens, with some independent chains.
Catenae	168	N-S/NNE	1625.7	9.4	• Crater chain, with craters interacting with each other.
U-shaped Trough	181	N-S/NE/E-W	2263.3	12.4	• Non-tectonic troughs. • Show underlying pit-crater chains in topographic data.
Chasmata	17	N-S/E-W	272.2	16	• Large mass-wasting chasms, often oval shaped.

We mapped a total of 81 pit-crater chains and 168 catenae (Table 3) across Ceraunius North, Ceraunius South and Tractus Fossae areas. We found both pit-crater chains and catenae among all three mapped fault groups either dotted through the landscape independently from the faults or located nested in between two graben-bounding faults (Figures 8a and 8b). The craters in the pit-crater chains vary between circular and oval in shape, with the long axis of the oval corresponding to the orientation of the chain itself. A portion of the pit-crater chains which are located within grabens show fault driven formation characteristics (e.g., en echelon distribution along strike, asymmetric pits etc.). The mapped pit-crater chains and catenae largely follow the N-S orientation of the majority of the faults in Group 2; however, there are instances of short pit-crater chains with a NNE/NE orientations (Figure 7).

The mapped u-shaped troughs appear as independent linear troughs or as branches from the large graben-forming faults, where they usually occur perpendicular to the main fault strike orientation. In the cross section, the troughs show steeply sloped sides (see Figure S1c in Supporting Information S1), and, unlike the linear grabens, the

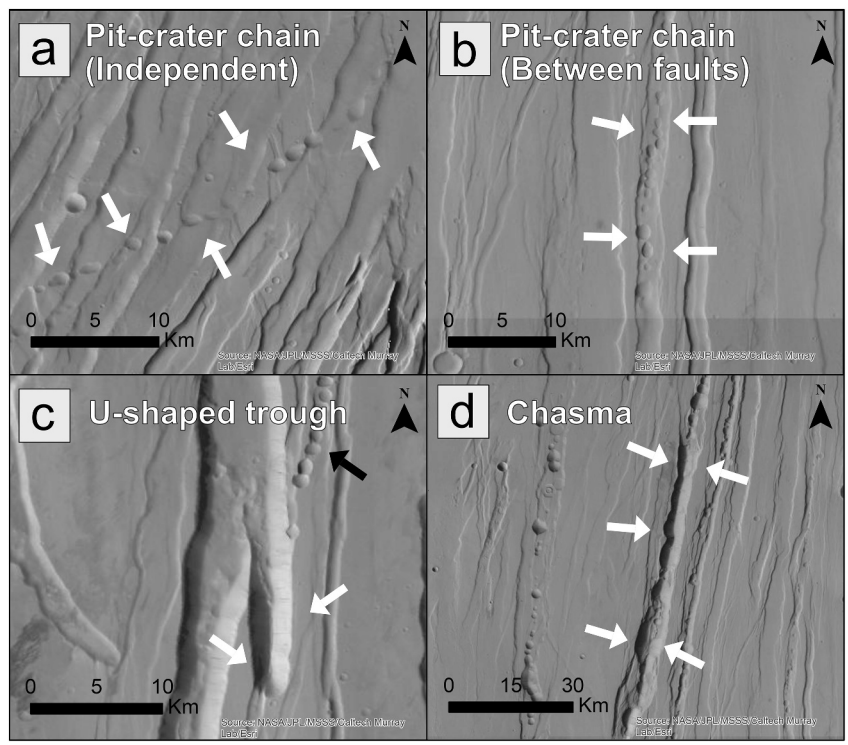

Figure 8. Example of (a) independent pit-crater chains (Type 1). Feature centered at 26°51′13.03″N, 105°38′22.07″W. (b) Example of a pit-crater chain located between two faults (Type 2). Feature centered at 24°15′14.42″N, 102°45′42.03″W. (c) U-shaped trough example (white arrows). The black arrow shows a pit-crater chain. Image centered at 25°55′13.23″N, 100°10′0.38″W. (d) Example of chasmata in Tractus Fossae (white arrows). Feature centered at 24°58′57.47″N, 103° 12′27.86″W. CTX Mosaic Credit: Esri, Caltech Murray Lab, NASA, JPL, MSSS.

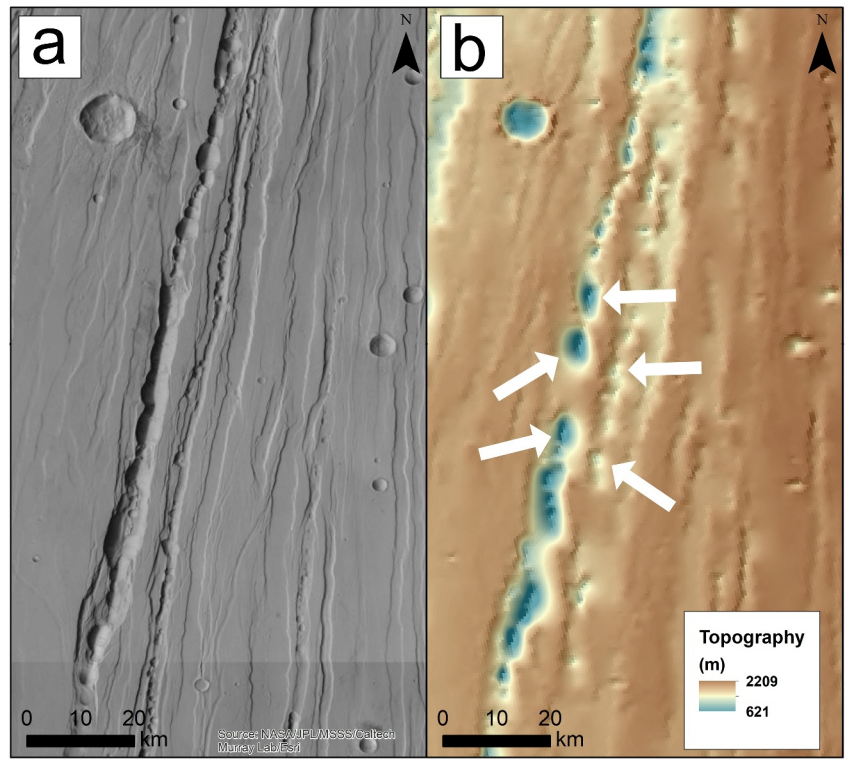

Figure 9. (a) Example of linear structures on CTX global mosaic image (Credit: Esri, Caltech Murray Lab, NASA, JPL, MSSS), which on (b) MOLA-HRSC blend topographic data overlaid with MOLA hillshade of the same area shows defined elongated crater morphologies of various sizes. MOLA-HRSC blend credit: Fergason et al. (2018).

troughs terminate in u-shapes, as in the example in Figure 8c. These features are found in all three study areas, but their large, striking, and complex appearance is the most evident in Tractus Fossae (Figure 7).

The final mapped collapse features are the chasmata, which appear as a combination of the pit-crater chains and the u-shaped troughs with their sharp but circular edges (Figure 9c). These are generally the largest features of the four identified groups and can be up to 70 km long and are found in all three study areas (Table 3).

Comparing the linear features mapped on the CTX images with the MOLA-HRSC blend topographic maps, the u-shaped troughs and chasmata both reveal instances of what appear to be craters or circular areas within the linear collapse features, which are much lower than the rest of the feature (Figure 9).

In summary, the collapse features are all observed either within narrow grabens, positioned parallel to narrow grabens, or perpendicular to narrow grabens. This relationship with grabens is especially true for the pit-crater chains; however, they also occasionally deviate from the orientation of the grabens. In cases where the independent pit crater chains and the grabens interact, the crosscutting relationships always suggest that the pit crater chains are younger, though the time between the two is undefined.

4. Discussion

4.1. Determining the Fault Groups

Fault mapping in our three study areas revealed a series of highly dense graben formations (Figure 4c). The faults are predominantly linear (Figure 5), though the northern section of Ceraunius North and Ceraunius South host faults, which exhibit a slight curvature, their shape suggesting a different extensional environment from the linear faults. Results from our work agree with previous studies (Cailleau et al., 2005; Tanaka, 1990) in that the first stage of faulting consisted of the NE striking faults, followed by an N-S oriented graben formation. We also define a third stage of activity younger than the NE and N-S orientations with our Group 3 NW oriented faults.

Table 4
Comparison of Previous (Tanaka et al., 2014) CSFD Ages, and the Ones Calculated in This Study (Unit Age)

Area name	Unit name	Prev. Age (Ga)	Unit age	Period
CERAUNIUS NORTH	*eHv*	3.65	1.4 ± 0.2 Ga	Middle Amazonian
CERAUNIUS SOUTH	*eHv*	3.65	2.2 ± 0.2 Ga	Early Amazonian
TRACTUS FOSSAE	*lHv*	3.55	2.4 ± 0.2 Ga	Early Amazonian

4.1.1. The Revised Ages of Ceraunius and Tractus Fossae

The absolute model ages calculated in this study using CSFD on the three study area units all resulted in Amazonian ages. This makes Ceraunius North 1 Ga younger than the other two units, and all three study areas 1–2 Ga younger than the previously reported ages by Tanaka et al. (2014) (Table 4).

Similar to the revised Ulysses Fossae ages (2.6 ± 0.2 Ga and 2.4 ± 0.2 Ga) determined by Shahrzad et al. (2023), our CSFD ages for southern Alba Mons are part of a significantly more detailed study of the craters in this specific area, when compared to ages from the global Tanaka et al. (2014) (Table 4). This focus on just three specific units enables more specific statistics when determining the ages of the units. The ages found in this study thus expectedly deviate from the previously determined ages (Table 4). However, the 1.4 Ga age for Ceraunius North is an outlier, and we considered the possibility of flooded craters potentially artificially lowering the age of Ceraunius North. However, after considering the morphology of the mapped craters, we did not observe sufficient evidence to attribute the exceptionally young unit age to flooded craters alone, though this remains a definite possibility. Considering the appearance of the three study areas, the younger age for Ceraunius North found in the results is not reflected in the appearance of the grabens, which are similar to the two other study areas.

With the long-term magma source in a single plate planetary system, it is likely that volcanoes have been periodically active in Tharsis between their Hesperian construction and their most recent caldera and resurfacing ages, which for some volcanoes continued into the Late Amazonian (Werner, 2009). For Pavonis Mons, the main edifice was constructed 3.65 Ga ago (Werner, 2009), with the most recent caldera CSFD ages as young as 130 Ma (Robbins et al., 2011) and 80 Ma (Werner, 2009). Ascreaus Mons was likewise constructed in the Hesperian, 3.65 Ga ago, with the most recent CSFD determined ages between 50 and 100 Ma from the flanks of the volcano. Additionally, there are CSFD determined Early Middle Amazonian ages of craters and resurfacing events for the Tharsis Montes, where a study by Werner et al. (2009) determined a strong Middle Amazonian resurfacing event for Pavonis Mons 1.2 Ga ago. This, along with Hesperian, Early, Middle and Late Amazonian flank and caldera ages for Ascreaus Mons, and Hesperian and Middle and Late Amazonian flank and caldera ages for Pavonis Mons, show evidence of a long-lived episodic history of volcanism for the Tharsis Montes. This is also the case for the giant radiating Tharsis dikes (e.g., Acheron, Phlegethon and Tractus Catenae), for which emplacement ages range between the Noachian and the Amazonian, based on the stratigraphic relationships between the structures (Wilson & Head, 2000).

For Ceraunius Fossae specifically, a study by Krishnan and Kumar (2023) determined a continuous history of volcanic eruptions during the entirety of the Late Amazonian. Though the majority of the studied lava flows were dated to the Late Amazonian, Krishnan and Kumar (2023) also identified Early to Middle Amazonian lava flows in Ceraunius Fossae. Again, this age is likely the reflection of the most recent activity, which marks the end of a long-lived period activity from a Ceraunius Fossae centered magmatic source. This is all consistent with the inferred longevity of the episodic magmatic and volcanic activity in Tharsis (e.g., Bleacher et al., 2009; Wilson et al., 2001). In terms of graben activity, studies by Ivanov and Head (2006) and more recently Krishnan and Kumar (2023) also looked at the Ceraunius Fossae grabens as a part of larger studies of the Alba Mons area. The former study determined a late Hesperian to early Amazonian age for radial graben formation in Ceraunius Fossae.

Comparing these studies to our crater counting results, it seems reasonable to suggest that the magmatic systems associated with Tharsis, and specifically the Tharsis Montes and Ceraunius Fossae, were active during the three periods determined in this study. The scarcity of Early to Middle Amazonian eruptive magmatic activity on the surface is likely a result of the extensive Late Amazonian volcanism (Christoph & Garry, 2017; Krishnan &

Kumar, 2023; Pieterek et al., 2022) covering earlier structures. It may also reflect a period during the Early and Middle Amazonian, where the majority of the magmatic activity was confined to the subsurface.

4.2. Fault Formation Mechanism

With defined groups and ages, we examine the morphology and appropriate stress fields which would be responsible for the orientation of the faults in order to evaluate the sources of the mapped faults. The mapped orientations of the faults suggest three distinct stress fields responsible for the three different orientations of faults in Ceraunius North, Ceraunius South and Tractus Fossae (Figure 5). The morphology of the faults in groups 1 and 2, and the linear faults in Group 3 (i.e., narrow grabens, uniform width and depth along strike, equal spacing between faults in the same group) along with their location in the highly active Tharsis volcanic province, enables our interpretation of mapped faults in our study forming as a result of diking (see Shahrzad et al., 2023, for a description of dike-induced graben formation mechanism). This is contrary to a purely tectonic extension origin, which usually manifests as much larger in width with fewer grabens over a similar area (Fernández & Ramírez-Caballero, 2019; Shahrzad et al., 2023). This interpretation is also aided by the orientation and location of the collapse features, which follow the paths of grabens in the groups. This is, however, not the case for the eastern curved faults in Group 3. These faults are wider spaced, and do not have any collapse features within the graben traces. We therefore reject a dike-origin for these faults and suggest a purely tectonic origin for the curved Group 3 faults. The formation of these features is further discussed in Section 4.4.3.

On Earth, these types of large scale igneous dike systems are observed as a part of large igneous provinces (LIPs) (Ernst et al., 2019), in areas such as the giant radiating Mackenzie dike swarm (a part of the Mackenzie Large Igneous Province on the Canadian Shield) and the Liberian dike swarm associated with the Central Atlantic Magmatic Province (Marzoli et al., 2018). Additionally, examples of dike-induced surface structures have been identified, where both dike geometry and the topography of paleosurfaces has been recognized. These examples are found in the Franklin-Natkusiak event in Canada (Rainbird, 1993), the Proterozoic event in Finland and NW Russia (Alapieti, 1982; Maier & Hanski, 2017), and most recently in 3D seismic reflection data in offshore NW Australia (Magee et al., 2023). Terrestrial dike swarms as a part of LIPs can reach distances similar to Martian dike swarms of >3,000 km. However, the duration of their emplacement is limited to a few million years (Ernst et al., 2001). We expect the Martian dike emplacement to have had a longer duration (>5 Ma) as the single-plate structure of the planet allows for magmatic activity to persist for much longer at the same locations.

4.3. Cavities Causing Observed Collapse Structures, Originating From Diking Processes

We mapped a significant number of collapse structures (pit-crater chains, catenae, u-shaped troughs and chasmata) in Ceraunius (North and South) and Tractus Fossae. Common for all four features are their relative younger ages, as all the features crosscut the faulting in the area. We consider the process that may have created them, and the connection to the surrounding faulting and their origins.

Our mapping revealed that the chasmata and u-shaped troughs both show patterns of pit-crater chains when examining the MOLA-HRSC topography in addition to the CTX images (Figure 9). Combining this with the erosional evolution from pit-crater chains to catenae, we consider the four collapse structures as 3–4 steps in the erosional evolution of an initial pit-crater chain (Figure 9a), an evolution initially suggested by Wyrick et al. (2004). This implies a common initial formation mechanism for all the structures, which evolves with time through different stages, resulting in with either a u-shaped trough or a chasma.

Previously, the collapse features have been explained by the collapse of material into subterranean cavities (Hardy, 2021). However, it is still disputed by which mechanism the cavities are created under the Martian surface. There are several proposed origins for cavity formation, with the most common two being (a) cavities due to the rapid withdrawal or volatile outgassing of magma in a dike (Mège et al., 2003; Scott et al., 2002), and (b) cavities produced by dilational faulting in cohesive material (Ferrill et al., 2011; Wyrick et al., 2004). To explore the feasibility of these origins, we consider our mapped collapse features.

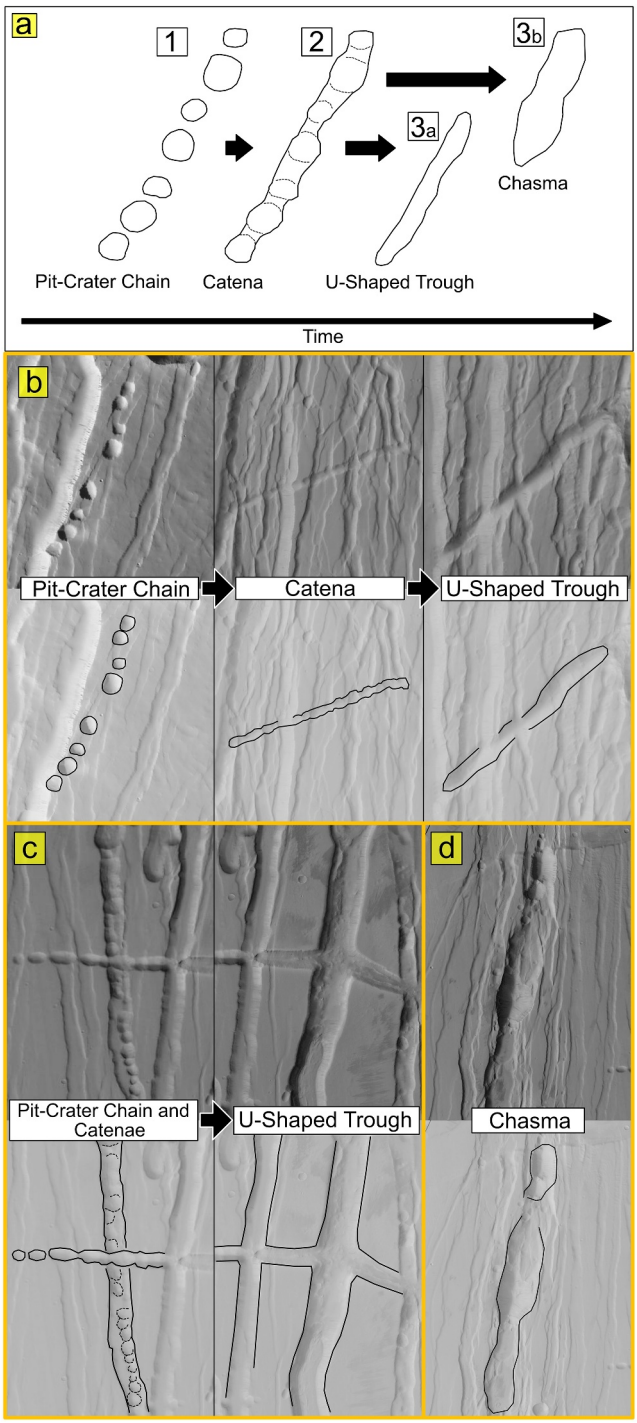

Figure 10. Overview of collapse structure evolution. (a) Evolution from Pit-crater chain to either u-shaped trough or chasma. (b) Examples of proposed pit-crater chain (feature centered at 29°39′32.34″N, 108°22′43.84″W) to catena (feature centered at 25°4′16.94″N, 106°24′2.90″W) and to u-shaped trough (feature centered at 24°18′32.85″N, 107°18′39.24″W) evolution, with CTX image on the top, and interpretation below. (c) Example of more complex trough development through intersecting PCC and catenae, with image centered at 26°41′23.8″N, 102°16′51.67″W. End result example of development is the complex troughs centered at 26°40′54.34″N, 102° 0′44.84″W (d) Example of Chasma, with feature located at 26°59′14.42″N,

4.3.1. Pit-Crater Chains and Catenae

Similar to Mège et al. (2003), we consider the catenae as an alignment of interacting pit-craters in a chain, and thus consider their formation from the same mechanism (Figures 10a and 10b). Our mapping showed two different types of pit-crater chains and catenae.

The first variety of pit-crater chains and catenae are found within the mapped grabens and follow their orientation along the strike (Figure 8b). The second variety of mapped PCCs and catenae do not appear within grabens, although the majority still follow the fault orientations. However, there are some examples of independent PCCs and catenae which do not follow the nearby fault orientations (Figure 8a). The size and shape of the craters are equally variable between the two types, but their orientations differ significantly. The PCCs from type 1 follow the exact orientation of the mapped grabens and are often located on the graben floor right along the side of a graben-bounding fault (See Figure 8b). These PCCs and catenae all follow the orientations of faults in Group 1, 2, and the linear faults in Group 3 (Table 4).

The remaining mapped PCCs and catenae are not bounded by any faults, yet they still follow the orientations of the fault in Group 1 or 2, either N-S or NNE. Because of the lack of surface faults or fractures associated with them, we cannot attribute these collapse features to extensional dilation fractures alone, based on the previous criteria (Cushing et al., 2015). However, we still determine them to be diking-induced, where the dikes producing the non-graben bound PCCs and catenae did not evolve sufficiently in order to induce any surface grabens.

Of the two common PCC formation theories, dike-induced and dilational faulting (e.g., Ferrill et al., 2011; Hardy, 2021; Wyrick et al., 2004), let us consider both theories. As mentioned, the PCCs display fault driven formation characteristics, which would suggest a tectonic origin. While the mapped PCCs are located in large-scale extensional environments, we have determined the source of the extensional faulting in the study area to be largely dike-driven. Dilational faulting is considered a purely tectonic process (Wyrick et al., 2004), where extension in a heterogeneous layered material allows unconsolidated material to fall into cavities developed in an underlying layer of more competent material. For the diking-related formation, volatile outgassing, magma withdrawal, or interactions with the cryosphere from an arrested dike-tip can produce cavities for the overlying material to collapse into (Scott et al., 2002; Wyrick et al., 2004). Depending on the ascending dike's development, this could occur coevally or post dike-induced graben formation. Both these options would explain the observed PCC formation. As we have determined pervasive diking in the area (i.e., the mapped graben) and instances of magmatic activity (e.g., Early to Late Amazonian lava flows mapped by Krishnan and Kumar (2023)), we consider it more likely for the formation of the mapped PCCs to be due to or related to the diking in the area. Whether the cavities are a result of dilational faulting produced by the arrested dike tips or from another process, for example, rapid withdrawal of magma or volatile outgassing, cannot be determined. However, we do reject the idea that our mapped pit-craters are a result of explosive eruptions from the ascending dikes, as we see no evidence of lava flow or eruptions associated directly with the mapped PCCs.

As the mapped PCCs are consistently younger than the grabens, we suggest that the PCC formation is related to later episodes of diking, where the magma has largely followed the paths of the graben-forming dikes. These later

episodes may have ascended to an even shallower depth than the previous dikes in order to create the cavities closer to the surface, and either (a) created further extensional faulting within the wider original grabens, where the path was already weakened, or (b) magma degassed in the subsurface, potentially due to interactions with ice or water, creating the cavity that enables the PCC formation.

4.3.2. U-Shaped Troughs and Chasmata

The orientation of the U-shaped troughs varies immensely, with some following the fault pattern and some changing orientation along the strike. This may reflect erosion between Type 1 and Type 2 pit-crater chains and catenae, as the example shown in Figure 10c. A recent study of Noctis Labyrinthus found that a volatile-rich layer (i.e., water ice) can facilitate the development from pit-craters to trough structures, specifically by the sublimation of a thermokarst layer (Kling et al., 2021). Further inspection of the mapped u-shaped troughs and chasmata in our study do show few (<5) instances of potential thermokarstic terrain (e.g., shallow, irregular depressions (Rodriguez et al., 2016)), but they are not pervasive enough to base our interpretation on. The intense erosion that has facilitated the u-shaped troughs and chasmata may then be attributed to the intense magmatic activity forming large and cohesive pit-crater chains, and the elevation of the units compared to the surroundings, having enabled more active erosion of the collapse features on the unit.

We interpret the chasmata as another end member of the PCC and catenae evolution chain, either as a 4th step following u-shaped trough formation or as a 3rd step following catenae formation bypassing the u-shaped trough formation (Figures 10a and 10d). This is a result of intense erosional formation, characterized by the large structure and evidence of mass-wasting along the interior of the chasmata. This facilitates the growth of the structure when the slopes become destabilized and induce landslides, widening the cavity (Mège et al., 2003). The large size (Table 4) of the mapped chasmata could also reflect a larger subsurface cavity than the PCCs, catenae and u-shaped troughs.

4.4. Considering the Origin of the Mapped Fault Groups

Assuming dike-related tectonic activity for the majority of our faults, we can thus identify two factors in their formation: the stress field in which the dikes have propagated and the source of the magma. As the study areas are located in an extremely large and active volcanic zone, there are a high number of magmatic and stress-field candidates.

4.4.1. Regional and Local E-W Stress Trajectories

Our initial approach is to broaden the scope and using a similar method to Shahrzad et al. (2023), where we investigate the graben orientations, and determine if they are radially fanning from any volcanic centers. Mapping geodesic radial paths from approximate volcanic centers near the study area (Alba Mons, Olympus Mons, the Tharsis Montes, etc.) shows no clear relationship between the mapped faults to a single volcanic center, particularly regarding the most prevalent fault group, Group 2 (Table 1). In a general sense, we can assign the N-S oriented faults in Ceraunius Fossae to lie in a radial orientation to Alba Mons, but this is not the case for the N-S faults in Tractus Fossae, where the closest radial orientation is from Ascraeus Mons (Figure 11). However, considering the lack of pervasive fault orientation and volcanic center relationships, we have many interacting stress fields from different orientations. These are both regional and local in scale, and in our study area, they all appear to produce N-S oriented fault structures. This means that there is either an E-W regional extensional field overpowering all other extension orientations or that the local and the regional stress fields are reinforcing each other. We therefore reconsider the main N-S orientation of the majority of our faults (Table 1) and determine the presence of a prevalent regional E-W extension regime over the entire study area.

The source of this E-W extension is likely regional stresses from the large-scale development of Tharsis, with potential assistance from any local extension from Alba Mons and Ascraeus Mons (Figure 10). This regional Tharsis extension, and the associated N-S oriented grabens have previously been attributed to a regional E-W Tharsis-wide extension driven by a stress field centered in Syria Planum, located to the south of the study areas (Plescia & Saunders, 1982; Tanaka, 1990). In the Tanaka (1990) study, the evolution is determined to originate with an initial isostatic doming, producing radial grabens proximal to the deformation center, which is then followed by a period of flexure, producing the distal grabens we see in

102°46′2.56″W. CTX background Global Mosaic credit: Esri, Caltech Murray Lab, NASA, JPL, MSSS.

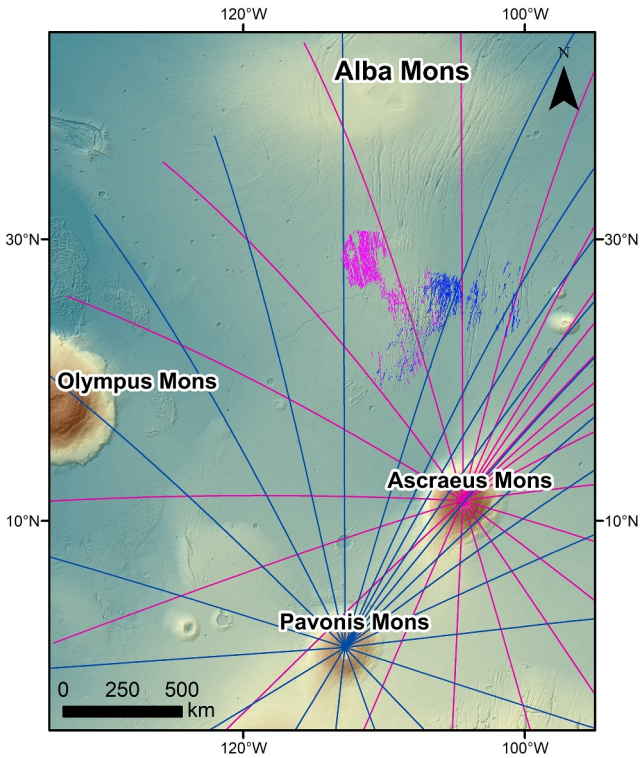

Figure 11. Projected geodesic radial faulting orientations from the two main volcanic edifices Pavonis Mons (blue) and Ascraeus Mons (pink) in relation to mapped fault groups, with Group 1 in blue and Group 3 in pink.

Ceraunius and Tractus Fossae (Tanaka, 1990). As we consider these features to be dike-related, Syria Planum could be a potential magma source, though we consider a more proximal source, such as Ceraunius Fossae or Alba Mons, more likely.

4.4.2. Magmatic Source

With this regional E-W extension in mind, we consider the source of magma for the propagating dikes. Further examining the study area in the context of the surrounding area, several features can be highlighted. First, both Ceraunius North and Ceraunius South (and to some degree Tractus Fossae) are at an elevated topography to the surrounding lava plains (Figure 12a). Second, Bouguer gravity maps of Mars (Genova et al., 2016) reveal two low density zones within Ceraunius North and South, with the lowest value of −288 mGal located in Ceraunius North (Figure 12b). Negative gravity anomalies can suggest underlying hotter and/or lower density crustal material and is such a useful indicator of the presence of plumes. Lastly, examining the global crustal thickness map of Mars (Genova et al., 2016), which accompanies the gravity data, we observe a zone of relatively higher crustal thickness (~20 km thicker) associated with the topographic highs (Figure 12c). This thicker crust may have increased the partial melting, generating ascending melts. This is, however, assuming that the current measured crustal thickness is similar to the thickness ~1.4 Ga. Note that these anomalies are not apparent for Tractus Fossae.

Together, along with the mapped dike-related faulting, these observations suggest a magma zone located underneath the Ceraunius Fossae area. These observations are also consistent with a more recent study by Plesa et al. (2023), which suggested several zones containing high melt fraction portions on Mars, which may still be active today. One of these identified high melt fraction (7%–8%) zones is located beneath Ceraunius Fossae, and is particularly pronounced in the scenario of a Mars with a crustal density difference between the Northern and Southern hemispheres (Plesa et al., 2023). This zone of magma is potentially a plume off-shoot from the Alba Mons plume or a zone of magmatic underplating. Both instances would be able to produce the vertically propagated dikes we have mapped in this study.

The 2023 study by Krishnan and Kumar examined boulders, pit-crater chains, lava flows, and select grabens in the Alba Mons area. Their findings concluded that magmatic underplating under Ceraunius Fossae was responsible for the small shield volcanism found in the area. Based on their surface ages, the study determines that the activity

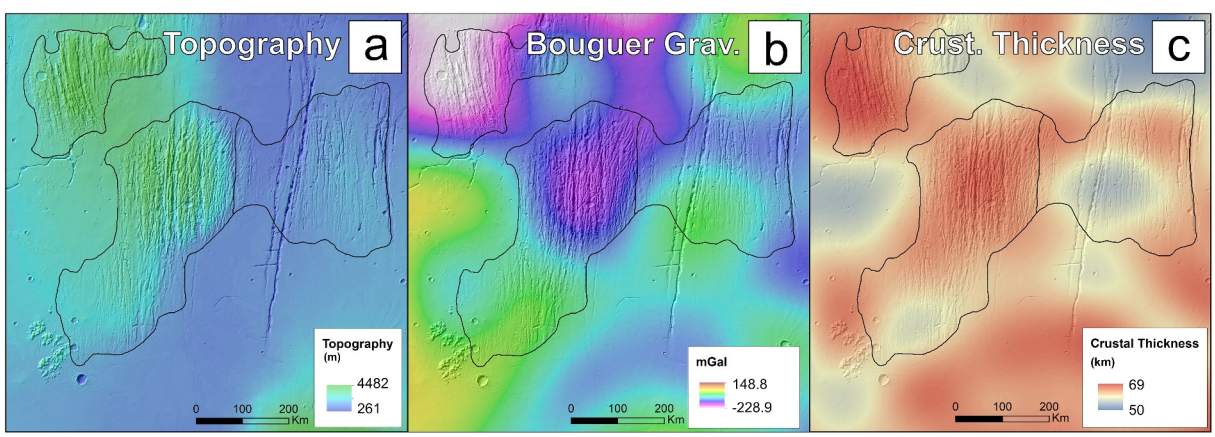

Figure 12. (a) MOLA Hillshade overlaid by merged MOLA-HRSC Digital Elevation model (200 m/px). Fergason et al. (2018) topographic map of Mars. (b) Bouguer gravity anomaly map for Mars (centered on study area) from Genova et al. (2016). (c) Crustal thickness map of Mars from Genova et al. (2016).

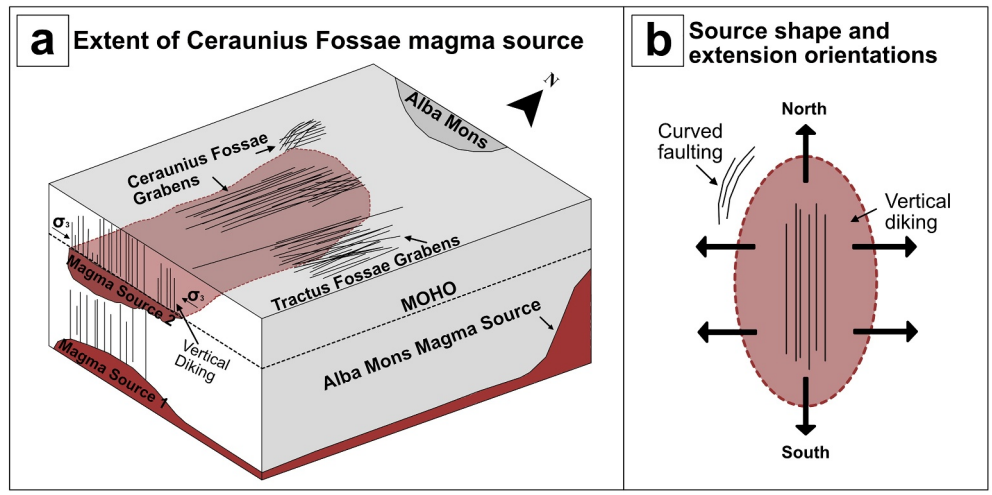

Figure 13. (a) Diagram of suggested Ceraunius Fossae magma source. Magma source 1 is the deep source feeding the shallower Magma Source 2, which in this model is magmatic underplating, but could also be a plume off-shoot from an Alba Mons plume. Vertical diking and thus the N-S grabens above the red Magma Source 2 area, is a result of the E-W extension from the magma source combined with a regional E-W extension. This results in N-S faulting immediately above (Ceraunius North and South) and east (Tractus Fossae) of the supposed Magma Source 2. (b) Shows a simplified suggestion of the magma source shape, and the surface faults the orientations of extension produced.

of this magma source has been migrating south during the Late Amazonian (Krishnan & Kumar, 2023). However, we suggest that the migration of the subsurface magmatic plumbing may have begun even earlier than this, emplacing dikes and subsequent grabens from the Early Middle Amazonian. This set the framework and was followed by the extensive period of surface eruptions in the Late Amazonian identified by Krishnan and Kumar (2023). This magmatic reservoir is likely an off-shoot or otherwise related to the larger Alba Mons plume (Krishnan & Kumar, 2023; Pieterek et al., 2022). Extension values also support a more directly intense extensional environment immediately above the recognized magma source, with 3.2% extension in Ceraunius South compared to the maximum 1.20% in the NS faults in Tractus Fossae. Considering the orientation of our mapped graben features, we suggest a pattern of vertically propagating dikes radially above a centralized Ceraunius Fossae magma source.

Figure 13 illustrates a potential Ceraunius Fossae centered magma source, in this case by underplating, as suggested by Krishnan and Kumar (2023). Another region of Tharsis has also been suggested to host a magmatic underplating source, in the southeast of Tharsis and west of the Tharsis Montes (Richardson et al., 2021). This particular magma source has been determined to be active within the last 500 Ma years (Richardson et al., 2021), supporting the longevity of the Tharsis magmatic activity.

A Ceraunius Fossae centered magma source scenario would explain the mapped N-S oriented grabens in Ceraunius Fossae but does not entirely justify the dike-induced grabens in Tractus Fossae. Though deformational centers related to magma chambers can vary laterally, for example, with an asymmetric magma chamber (Gudmundsson, 2020), we suggest that a combination of E-W radial stresses on the surface above the magma chamber, along with any E-W radial extension fields radiating from the Alba Mons and Ascraeus Mons volcano-tectonic centers, are responsible for the N-S oriented faults in Tractus Fossae. The overlapping E-W stress fields from Alba Mons, Ascraeus Mons and likely Syria Planum reinforced each other and facilitated the vertical diking in Tractus Fossae from a Ceraunius Fossae centered magma source.

4.4.3. Sources of Extensional Stresses for Each Fault Group

Considering these stress trajectories and potential magma sources presented, we determined the source of extensional stresses for the mapped fault groups.

Group 1: An exact source for the stresses responsible for Group 1 is difficult to determine with certainty, as the combination of location and orientation can result from a number of extensional events. The faults in Group 1 follow an NNE orientation. We have determined the extension to be dike-induced, which corresponds to the

orientation of the largest collapse features mapped in this study. With this in mind, we consider the orientation of the features surrounding Alba Mons. Acheron and Phlegethon Catena, located on the SE flank of Alba Mons (Figure 1), are both parallel in orientation to the mapped Group 1 faults with an NNE strike. These two Catenae are considered the surface expressions of dikes (Raitala, 1988; Scott et al., 2002). This is also the case, as suggested for Tractus Catena (see location on Figure 1), which we have also identified as a collapse structure in this study. A study by Mège et al. (2003) likewise suggested a dike-induced origin for the catena. The similar orientation and collapse-induced morphology between the mapped faults in our study and the origins for Acheron, Phlegethon, and Tractus Catena suggests a correlation between their origins. This would put Group 1 faults in the same system of Tharsis radial dikes, which have driven the formation of large grabens with similar orientation during the Middle Amazonian (Okubo & Schultz, 2005; Scott et al., 2002).

In addition to the Tharsis-radial scale diking, we also consider the effect of large volcanic edifices located within ~1,000 km radius from the study area. Considering the radial patterns using the volcanic edifices as an approximate center of deformation, Group 1 faults have the best fit with projected radial orientations from Pavonis Mons (Figure 10). Robbins et al. (2011) determined a Pavonis Mons summit caldera age as young as 130 ± 20 Ma, which together with the Early Amazonian Pavonis Mons activity recorded by Bouley et al. (2018), suggests a (likely periodical) history of magmatic activity which continued through the Amazonian. This corresponds to the early Amazonian maximum age for Group 1 determined in this study. We therefore propose an origin for the Group 1 faults, related to NNE diking and oriented by Pavonis radial stresses, which may have been emphasized by crustal weakening associated with previous large-scale Tharsis radial diking.

Group 2: The Ceraunius Fossae part of Group 2 grabens (Figure 5) is the result of vertical diking, likely from a local plume or magmatic underplating source (Figure 13a). For reasons discussed above, Tractus Fossae appears different as it lacks the evidence of a low-density anomaly underneath and is thus not considered to be located directly above the magma source. The extensive N-S diking in Group 2 is likely the result of several interacting stress fields, namely the regional Tharsis E-W extension, and E-W extension related to Alba Mons and Ascraeus Mons, though we still consider an Alba Mons plume or the potential Ceraunius Fossae underplating as the source of the dikes, with the surrounding extensions explaining the dike orientations.

A highlighted feature of this group is the high density of faulting (Figure 4c) in Ceraunius South. We consider it a likely overprinting of several stages of largely N-S oriented faulting, which are near-impossible to distinguish from each other.

Group 3: The majority of the faults mapped in this group are in Ceraunius North, and it contains both linear and a portion of curved faults. Curved faults are found in several places on Mars, such as the Alba Fossae around Alba Mons (Öhman & McGovern, 2014), and around other volcanoes such as Labeatis Mons (Orlov et al., 2022). Common for these, is that the structures all curve around a volcanic center, which is not the case for the northern Group 3 faults. As discussed above, we do not consider these faults dike related, a theory which is strengthened by the lack of collapse features which follow the orientation of the faults. As there are no signs of a buried volcanic structure near the faults, we consider their origin a more likely result from interacting stress fields. However, instead of reinforcing each other, as in the case with Tractus Fossae, they change the orientation of the structure.

Figure 12b shows a suggestion on how this may occur. Here we assume an elongated magma source, where the bounding extension stresses result in curved grabens. Curved grabens are also indicative of either loading or deflation associated with a volcanic center (Cailleau et al., 2003; Mège & Masson, 1996). On Earth, this is referred to as a "wristwatch pattern," and can be found around volcanoes such as Fantale in the Afar rift, and Hengill in Iceland (van Wyk de Vries & Matela, 1998). It is also present on Venus, where Kvasha Patera displays a clear example of the circumferential structure (Cyr & Melosh, 1993). As mentioned, we do not observe any structure the faults would be circumferential to, but deflation of a volcanic center (e.g., by cooling or magma withdrawal), consequently covered by more recent lava flows, remains another possibility. The reason for the limited spatial occurrence of the curved Group 3 faults may reflect a more shallow portion of the magmatic source driving the extension, aided by any pre-existing weaknesses as a result of the evolution of Alba Mons (Cailleau et al., 2003). Additional modeling of the proposed Ceraunius Fossae magma source is needed to confirm this.

The linear NNW trending faults in this group have collapse features in the same orientation, and within the grabens, and their radial orientation to the nearby Ascraeus Mons suggests diking related activity as the source of these faults. Ascreaus Mons is located an approximate 800 km from the center of Ceraunius North (Figure 11),

which would reflect the travel distance of potential radial dikes. In Tharsis, radiating dikes have been determined to travel as far as 1,000 km (Scott et al., 2002) with a maximum distance of 3,000–4,000 km (Wilson & Head, 2000) from their source. We find similar examples on Earth, where the largest fanning dike swarm, the Mackenzie swarm, contains dikes that have traveled nearly 2,500 km (Ernst et al., 2001). The linear and curved faults in Group 3 appear side-by-side, so their slight change in orientation cannot be distinguished temporally.

4.5. Stages of Deformation South of Alba Mons

We have identified four main stages of structural activity in Ceraunius Fossae and Tractus Fossae, all occurring in the Amazonian. Based on their ages and orientations, we propose the following stages of evolution of the southern area of Alba Mons (Figure 14).

1. Following an Amazonian lava emplacement, laterally propagating radial dikes from a volcanotectonic center near the mid of the Tharsis bulge reflect the first recorded extension activity in Ceraunius South and Tractus Fossae. WNW-ESE extension facilitates NNE trending faults in Tractus Fossae and Ceraunius South (Figure 14a). These diking induced grabens are likely sourced from either Pavonis Mons or a center in Tharsis itself.
2. Previous regional E-W extension related to the isostatic loading of Syria Planum has likely weakened the crust in Ceraunius Fossae and Tractus Fossae, and thus aided the emergence of Alba Mons plume/Ceraunius Fossae underplating sourced vertical diking-induced faulting (Figure 14b). This E-W extension that allowed the intensity of the N-S faulting was likely amplified by radial stresses from Alba Mons and Ascraeus Mons.
3. Activity from the Ceraunius Fossae magma source, perhaps related to late-stage deflation in accordance with diminishing activity, creates a set of curved faults to the south of Alba Mons (Figure 14c).
4. Any low-lying lands are covered with the most recent Amazonian lava flows (unit AHv on Figure 3) (Tanaka et al., 2014), isolating the raised patches we map in this study (Figure 14d). Smaller instances of tectonic activity may have continued after this period, with few (∼12) identified grabens within the study area dated between 1.9 Ga and 45 Ma based on their contact with dated lava flows (Krishnan & Kumar, 2023).

4.6. Implications for Magma Reservoir Location

Results from the fault mapping and grouping reveal three main stages of extensional activity in Ceraunius and Tractus Fossae, occurring during the Amazonian. Overall, the area south of Alba Mons shows intense surface deformation, the majority of which is associated with the magmatic activity localized here. We observe extensional faulting as a result of diking, and collapse features such as pit-crater chains, which we consider the result of arrested dikes interacting with the surface. As mentioned in the introduction, the magma that fed the extensive diking and subsequent extensional faulting and collapse structures around the surface of Alba Mons is suggested to originate from a separate source, independent of the Tharsis superplume.

Other highly faulted volcanotectonic areas, such as Ulysses Fossae (Fernández & Ramírez-Caballero, 2019; Shahrzad et al., 2023) and Noctis Labyrinthus (Kling et al., 2021), display similar pit-crater chain and catenae morphology as the ones we have mapped south of Alba Mons in this study. However, the complexity of troughs varies between the three locations in a range from least to most amount of structure complexity. Ulysses Fossae show the least amount of trough complexity, where the few instances of collapse structures are isolated PCCs and troughs, with only a few contained compound trough structures in the northern part (Shahrzad et al., 2023). An increase in complexity is found in the examples in this study, where Ceraunius and Tractus Fossae show more "developed" structures, interlinking u-shaped troughs, catenae and PCCs. Then, the intricate chaotic terrain and interacting troughs in Noctis Labyrinthus define the majority of the structures there (Kling et al., 2021), and show the most complex collapse structures between the three examples.

Particularly for the Alba Mons hotspot, a study by Ivanov and Head (2006) concluded that the magma reservoir feeding the Alba Mons lobes must be located at a relatively shallow depth (high topographic level) compared to other Tharsis volcanoes. Additionally, Mège et al. (2003) investigated representative areas of Alba Mons and Noctis Labyrinthus, and found that magma reservoirs might lie at ∼1 and ∼5 km depth, respectively. These findings could indicate that the source of magma was relatively close to the surface, compared to the rest of the Tharsis volcanoes and could thus have an influence on the amount and longevity of the diking, and the subsequent high-density faulting and collapse structures, which compared to Ulysses Fossae, are more prevalent in Ceraunius and Tractus Fossae as well as Noctis Labyrinthus. This magma source may have remained stable throughout the

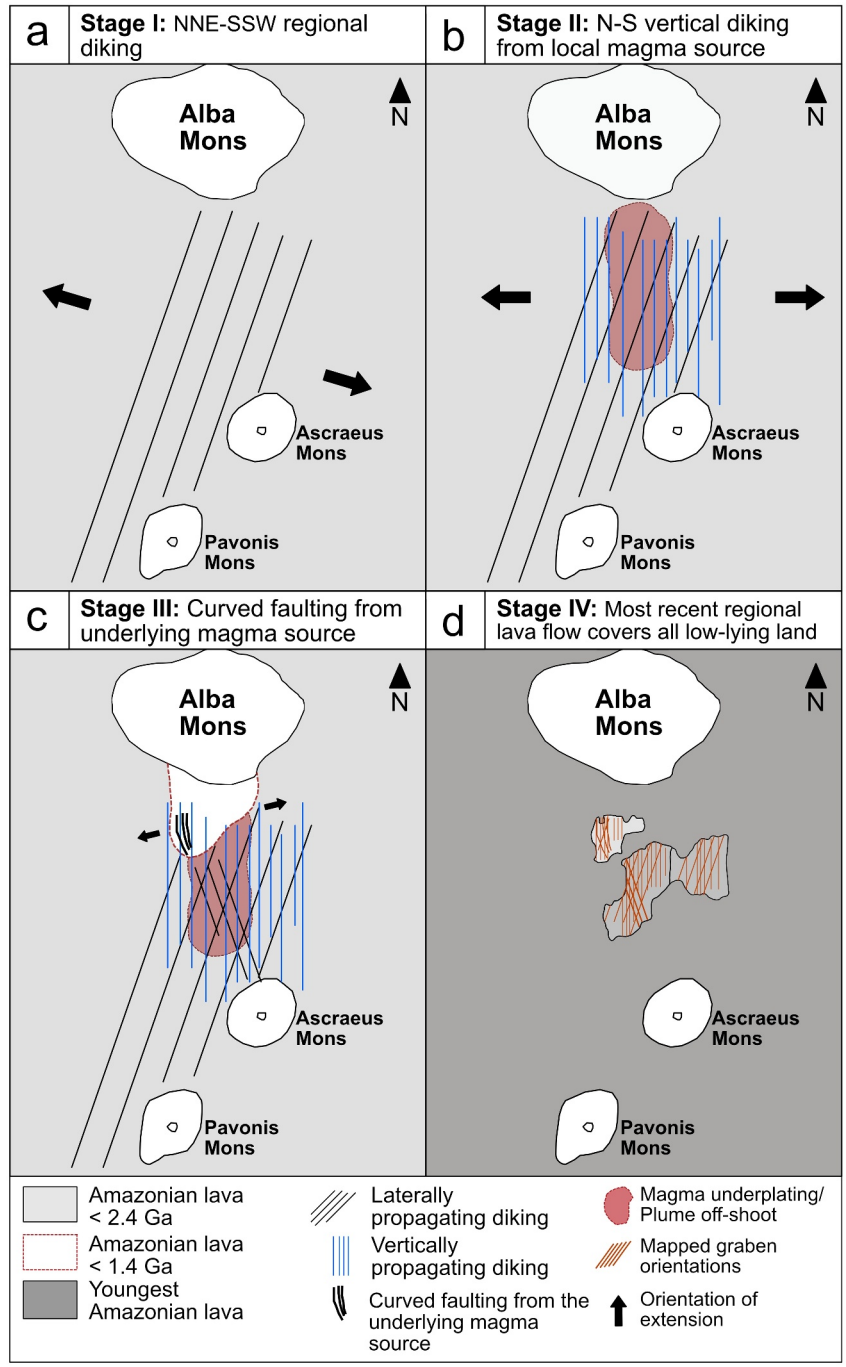

Figure 14. The four main stages of tectonic activity in the southern Alba Mons, all occurring during the Amazonian. (a) Stage I, initial WSW/ESE extension, due to Tharsis bulge centered diking, which results in NNE oriented grabens. (b) Stage II, activity from Ceraunius Fossae centered magma source, combined with regional (Syria Planum centered) and local (Alba Mons and Ascraeus Mons) E-W extension produces N-S oriented vertical diking. (c) Stage III, interacting stress fields from the Ceraunius Fossae magma source, together with Ascraeus Mons diking produces linear and curved faulting. (d) The most recent Amazonian lava flow covers all low-lying terrain.

Amazonian, with potential remnants of this reservoir still located underneath Ceraunius Fossae at present day, as suggested by Plesa et al. (2023). Other Tharsis volcanoes such as the Tharsis Montes show pit-crater chain structures on the flanks of the volcanoes, but given the distance from the main volcano for the faults in Noctis Labyrinthus (Kling et al., 2021) and Ceraunius and Tractus Fossae, a relatively more shallow magma source (and

near-surface volatile layers) could be the reason for the complexity of the collapse structures in those locations, compared to Ulysses Fossae (Shahrzad et al., 2023). There, the comparative "lack" of complex collapse features from the majority of the Tharsis-superplume related volcanoes, could reflect a deeper magma source. However, this is just one possible explanation and further modeling of the potential magmatic reservoirs is necessary to confirm or refute it.

5. Conclusions

- In this study, we mapped and measured ~12,000 faults and determined their ages of activity based on crater size-frequency model ages, as being active during the Amazonian period, late in Mars' history.
- Grouping the faults based on orientation and morphology reveals three distinct stages of extensional activity recorded in the study areas, with a change from NE to N-S to NW oriented faults and associated perpendicular extensional strain orientations through time.
- We determine the majority of the faulting to be dike-induced (groups 1, 2 and some of 3) with both regional (Tharsis) and local (Alba Mons, Ascraeus Mons and Pavonis Mons) centers of deformation. We determine the curved western faults in Group 3 to be purely tectonic and a result of the stresses from a local magmatic source.
- Additionally, the mapped collapse structures are also considered related to diking and are consistently younger than the mapped faults.
- The magmatic activity from a local Ceraunius Fossae magma source (either from an Alba Mons plume off-shoot, or magmatic underplating), has highly influenced Ceraunius and Tractus Fossae, with dike-induced graben formation and associated pit-crater chains, catenae, u-shaped troughs and chasmata dotting the landscape. This potentially shallow and recent (<1.4 Ga) magmatic activity was inducive to the mapped surface deformation, which was amplified by the regional Tharsis E-W extension, with influence from radial stresses from local volcanoes.

Data Availability Statement

Mapped faults, collapse features, and craters from this study are available to download free from Zenodo: faults (Shahrzad, 2023a), collapse features (Shahrzad, 2023b), and craters (Shahrzad, 2023c). The CTX global mosaic (Credit: Esri, Caltech Murray Lab, NASA, JPL, MSSS) used in this study can be downloaded from The Murray Lab's website at https://murray-lab.caltech.edu/CTX/ and the MOLA-HRSC DEM v2 used to generate topographic profiles is available from the USGS Astropedia Catalog (Fergason et al., 2018). The software used in this research is available to download for free: Craterstats 2.0 is available from the Freie Universität Berlin at https://www.geo.fu-berlin.de/en/geol/fachrichtungen/planet/software/index.html and FracPaQ (Healy et al., 2017) is available for download via GitHub.

Acknowledgments
S. Shahrzad is funded by the National Environmental Research Council (NERC) Panorama Doctoral Training Partnership NE/S007458/1. We thank NASA and ESA for the free access to Martian data through NASA's Planetary Data System (PDS). We thank reviewers Teemu Öhman and one anonymous reviewer for their feedback, which has greatly improved this work.

References

Alapieti, T. (1982). The Koillismaa layered igneous complex, Finland: Its structure, mineralogy and geochemistry, with emphasis on the distribution of chromium. *Geological Survey of Finland Bulletin*, *319*, 116. https://tupa.gtk.fi/julkaisu/bulletin/bt_319.pdf

Banerdt, W. B., Golombek, M. P., & Tanaka, K. L. (1992). Stress and tectonics on Mars. In H. H. Kieffer, B. M. Jakosky, C. W. Snyder, & M. S. Matthews (Eds.), *Mars* (pp. 249–297). University of Arizona Press.

Belleguic, V., Lognonné, P., & Wieczorek, M. (2005). Constraints on the Martian lithosphere from gravity and topography data. *Journal of Geophysical Research*, *110*(E11). https://doi.org/10.1029/2005JE002437

Bleacher, J. E., Glaze, L. S., Greeley, R., Hauber, E., Baloga, S. M., Sakimoto, S. E. H., et al. (2009). Spatial and alignment analyses for a field of small volcanic vents south of Pavonis Mons and implications for the Tharsis province, Mars. *Journal of Volcanology and Geothermal Research*, *185*(1), 96–102. https://doi.org/10.1016/j.jvolgeores.2009.04.008

Borraccini, F., Lanci, L., & Wezel, F. C. (2006). Does a detachment level exist beneath the Ceraunius Fossae? Insights from graben mapping and lost-area balancing analysis. *Planetary and Space Science*, *54*(7), 701–709. https://doi.org/10.1016/j.pss.2006.03.004

Borraccini, F., Lanci, L., Wezel, F. C., & Baioni, D. (2005). Crustal extension in the Ceraunius Fossae, Northern Tharsis Region, Mars. *Journal of Geophysical Research*, *110*(6), 1–10. https://doi.org/10.1029/2004JE002373

Bouley, S., Baratoux, D., Paulien, N., Missenard, Y., & Saint-Bézar, B. (2018). The revised tectonic history of Tharsis. *Earth and Planetary Science Letters*, *488*, 126–133. https://doi.org/10.1016/j.epsl.2018.02.019

Byrne, P. K., Holohan, E. P., Kervyn, M., van Wyk de Vries, B., & Troll, V. R. (2015). Analogue modelling of volcano flank terrace formation on Mars. *Geological Society*, *401*(1), 185–202. https://doi.org/10.1144/SP401.14

Cailleau, B., Walter, T. R., Janle, P., & Hauber, E. (2003). Modeling volcanic deformation in a regional stress field: Implications for the formation of graben structures on Alba Patera, Mars. *Journal of Geophysical Research*, *108*(E12). https://doi.org/10.1029/2003JE002135

Cailleau, B., Walter, T. R., Janle, P., & Hauber, E. (2005). Unveiling the origin of radial grabens on Alba Patera volcano by finite element modelling. *Icarus*, *176*(1), 44–56. https://doi.org/10.1016/j.icarus.2005.01.017

Carr, M. H. (1974). Tectonism and volcanism of the Tharsis Region of Mars. *Journal of Geophysical Research (1896-1977)*, *79*(26), 3943–3949. https://doi.org/10.1029/JB079i026p03943

Christoph, J. M., & Garry, W. B. (2017). Spatial and temporal relationships among low shield volcanoes in the Ceraunius Fossae Region of Tharsis: The last gasp of Martian volcanism. In *Presented at 48th Annual Lunar and Planetary Science Conference (2017)* (p. 2798).
Cushing, G. E., Okubo, C. H., & Titus, T. N. (2015). Atypical pit craters on Mars: New insights from THEMIS, CTX, and HiRISE observations. *Journal of Geophysical Research: Planets*, *120*(6), 1023–1043. https://doi.org/10.1002/2014JE004735
Cyr, K. E., & Melosh, H. J. (1993). Tectonic patterns and regional stresses near Venusian Coronae. *Icarus*, *102*(2), 175–184. https://doi.org/10.1006/icar.1993.1042
Dohm, J. M., Baker, V. R., Maruyama, S., & Anderson, R. C. (2007). Traits and evolution of the Tharsis superplume, Mars. In D. A. Yuen, S. Maruyama, S.-I. Karato, & B. F. Windley (Eds.), *Superplumes: Beyond plate tectonics* (pp. 523–536). Springer. https://doi.org/10.1007/978-1-4020-5750-2_17
Ernst, R. E., Grosfils, E., & Mège, D. (2001). Giant Dike Swarms: Earth, Venus, and Mars. *Annual Review of Earth and Planetary Sciences*, *29*(1), 489–534. https://doi.org/10.1146/annurev.earth.29.1.489
Ernst, R. E., Liikane, D. A., Jowitt, S. M., Buchan, K. L., & Blanchard, J. A. (2019). A new plumbing system framework for mantle plume-related continental Large Igneous Provinces and their mafic-ultramafic intrusions. *Journal of Volcanology and Geothermal Research*, *384*, 75–84. https://doi.org/10.1016/j.jvolgeores.2019.07.007
Fergason, R. L., Hare, T. M., & Laura, J. (2018). HRSC and MOLA blended digital elevation model at 200m v2. [Map] [Dataset]. *Astrogeology PDS Annex, U.S. Geological Survey*. https://arcg.is/1OOm9K
Fernández, C., & Ramírez-Caballero, I. (2019). Evaluating transtension on Mars: The case of Ulysses Fossae, Tharsis. *Journal of Structural Geology*, *125*, 325–333. https://doi.org/10.1016/j.jsg.2018.05.009
Ferrill, D. A., Wyrick, D. Y., & Smart, K. J. (2011). Coseismic, dilational-fault and extension-fracture related pit chain formation in Iceland: Analog for pit chains on Mars. *Lithosphere*, *3*(2), 133–142. https://doi.org/10.1130/L123.1
Genova, A., Goossens, S., Lemoine, F. G., Mazarico, E., Neumann, G. A., Smith, D. E., & Zuber, M. T. (2016). Seasonal and static gravity field of Mars from MGS, Mars Odyssey and MRO radio science. *Icarus*, *272*, 228–245. https://doi.org/10.1016/j.icarus.2016.02.050
Gudmundsson, A. (2020). Magma movement through the crust: Dike paths. In *Volcanotectonics: Understanding the structure, deformation and dynamics of volcanoes* (pp. 325–378). Cambridge University Press.
Hardy, S. (2021). Discrete element modelling of pit crater formation on Mars. *Geosciences*, *11*(7), 268. https://doi.org/10.3390/geosciences11070268
Hartmann, W. K. (2005). Martian cratering 8: Isochron refinement and the chronology of Mars. *Icarus*, *174*(2), 294–320. https://doi.org/10.1016/j.icarus.2004.11.023
Hartmann, W. K., & Daubar, I. J. (2016). Martian cratering 11. Utilizing decameter scale crater populations to study Martian history. *Meteoritics and Planetary Sciences*, *52*(3), 493–510. https://doi.org/10.1111/maps.1280
Hauber, E., Brož, P., Jagert, F., Jodłowski, P., & Platz, T. (2011). Very recent and wide-spread basaltic volcanism on Mars. *Geophysical Research Letters*, *38*(10). https://doi.org/10.1029/2011GL047310
Healy, D., Rizzo, R. E., Cornwell, D. G., Farrell, N. J. C., Watkins, H., Timms, N. E., et al. (2017). FracPaQ: A MATLAB™ toolbox for the quantification of fracture patterns. *Journal of Structural Geology*, *95*, 1–16. https://doi.org/10.1016/j.jsg.2016.12.003
Ivanov, M. A., & Head, J. W. (2006). Alba Patera, Mars: Topography, structure, and evolution of a unique late Hesperian–early Amazonian shield volcano. *Journal of Geophysical Research*, *111*(E9). https://doi.org/10.1029/2005JE002469
Janle, P., & Erkul, E. (1991). Gravity studies of the Tharsis area on Mars. *Earth, Moon, and Planets*, *53*(3), 217–232. https://doi.org/10.1007/BF00055948
Jenness, J. (2011). *Tools for graphics and shapes: Extension for ArcGIS (version 2.1.85)*. Jenness Enterprises. Retrieved from http://www.jennessent.com/arcgis/shapes_graphics.htm
Kling, C. L., Byrne, P. K., Atkins, R. M., & Wegmann, K. W. (2021). Tectonic deformation and volatile loss in the formation of Noctis Labyrinthus, Mars. *Journal of Geophysical Research: Planets*, *126*(11), e2020JE006555. https://doi.org/10.1029/2020JE006555
Kneissl, T., van Gasselt, S., & Neukum, G. (2011). Map-projection-independent crater size-frequency determination in GIS environments—New software tool for ArcGIS. *Planetary and Space Science*, *59*(11), 1243–1254. https://doi.org/10.1016/j.pss.2010.03.015
Krishnan, V., & Kumar, P. S. (2023). Long-lived and continual volcanic eruptions, tectonic activity, pit chains formation, and boulder avalanches in Northern Tharsis Region: Implications for late amazonian geodynamics and seismo-tectonic processes on Mars. *Journal of Geophysical Research: Planets*, *128*(1), e2022JE007511. https://doi.org/10.1029/2022JE007511
Magee, C., Love, V., Fayz, K., Andrews, B., Rivas-Dorado, S., Jackson, C., et al. (2023). Quantifying dyke-induced Graben and Dyke structure using 3D seismic reflection data and the role of interpretation bias. *Tektonika*, *1*(2). https://doi.org/10.55575/tektonika2023.1.2.25
Maier, W. D., & Hanski, E. J. (2017). Layered mafic–ultramafic intrusions of Fennoscandia: Europe's Treasure chest of magmatic metal deposits. *Elements*, *13*(6), 415–420. https://doi.org/10.2138/gselements.13.6.415
Marzoli, A., Callegaro, S., Dal Corso, J., Davies, J., Chiaradia, M., Youbi, N., et al. (2018). The central Atlantic magmatic province (CAMP): A review. In L. H. Tanner (Ed.), *The late Triassic World* (pp. 91–125). Springer. https://doi.org/10.1007/978-3-319-68009-5_4
McGovern, P. J., Solomon, S. C., Head, J. W., III., Smith, D. E., Zuber, M. T., & Neumann, G. A. (2001). Extension and uplift at Alba Patera, Mars: Insights from MOLA observations and loading models. *Journal of Geophysical Research*, *106*(E10), 23769–23809. https://doi.org/10.1029/2000JE001314
Mège, D. (1999). Dikes on Mars: (1) what to look for? (2) A first survey of possible dikes during the Mars global surveyor aerobreaking and science phasing orbits. In *Paper presented at Fifth International Conference on Mars* (p. 6207).
Mège, D., Cook, A. C., Garel, E., Lagabrielle, Y., & Cormier, M. H. (2002). Surface collapse and volcanic rifting on Mars (abstract). In *Proceedings of the Lunar and Planetary Science Conference* (33rd ed., p. 2042).
Mège, D., Cook, A. C., Garel, E., Lagabrielle, Y., & Cormier, M.-H. (2003). Volcanic rifting at Martian grabens. *Journal of Geophysical Research*, *108*(E5), 5044. https://doi.org/10.1029/2002JE001852
Mège, D., & Masson, P. (1996). A plume tectonics model for the Tharsis province, Mars. *Planetary and Space Science*, *44*(12), 1499–1546. https://doi.org/10.1016/S0032-0633(96)00113-4
Michael, G. G. (2013). Planetary surface dating from crater size–frequency distribution measurements: Multiple resurfacing episodes and differential isochron fitting. *Icarus*, *226*(1), 885–890. https://doi.org/10.1016/j.icarus.2013.07.004
Michael, G. G., Kneissl, T., & Neesemann, A. (2016). Planetary surface dating from crater size-frequency distribution measurements: Poisson timing analysis. *Icarus*, *277*, 279–285. https://doi.org/10.1016/j.icarus.2016.05.019
Öhman, T., & McGovern, P. J. (2014). Circumferential graben and the structural evolution of Alba Mons, Mars. *Icarus*, *233*, 114–125. https://doi.org/10.1016/j.icarus.2014.01.043
Okubo, C. H., & Schultz, R. A. (2005). Evidence of Tharsis-radial dike intrusion in southeast Alba Patera from MOLA-based topography of pit crater chains. In *Proceedings of the Lunar and Planetary Science Conference* (36th ed., p. 1007).

Orlov, C. J., Bramham, E. K., Thomas, M., Byrne, P. K., Piazolo, S., & Mortimer, E. (2022). Structural architecture and deformation history of Tempe Terra, Mars. *Journal of Geophysical Research: Planets*, *127*(11), e2022JE007407. https://doi.org/10.1029/2022JE007407

Pieterek, B., Ciazela, J., Lagain, A., & Ciazela, M. (2022). Late Amazonian dike-fed distributed volcanism in the Tharsis volcanic province on Mars. *Icarus*, *386*, 115151. https://doi.org/10.1016/j.icarus.2022.115151

Plesa, A.-C., Wieczorek, M., Knapmeyer, M., Rivoldini, A., Bozdag, E., Walterova, M., et al. (2023). InSight's constraints on the interior of Mars: Geodynamical models and observations. In *Proceedings of the Lunar and Planetary Science Conference* (54th ed., p. 2212).

Plescia, J. B. (1994). Geology of the small Tharsis volcanoes: Jovis Tholus, Ulysses Patera, Biblis Patera, Mars. *Icarus*, *111*(1), 246–269. https://doi.org/10.1006/icar.1994.1144

Plescia, J. B. (2004). Morphometric properties of Martian volcanoes. *Journal of Geophysical Research*, *109*(E3), E03003. https://doi.org/10.1029/2002JE002031

Plescia, J. B., & Saunders, R. S. (1982). Tectonic history of the Tharsis region, Mars. *Journal of Geophysical Research*, *87*(B12), 9775–9791. https://doi.org/10.1029/JB087iB12p09775

Polit, A. T., Schultz, R. A., & Soliva, R. (2009). Geometry, displacement–length scaling, and extensional strain of normal faults on Mars with inferences on mechanical stratigraphy of the Martian crust. *Journal of Structural Geology*, *31*(7), 662–673. https://doi.org/10.1016/j.jsg.2009.03.016

Rainbird, R. H. (1993). The sedimentary record of mantle plume uplift preceding eruption of the neoproterozoic natkusiak flood basalt. *The Journal of Geology*, *101*(3), 305–318. https://doi.org/10.1086/648225

Raitala, J. (1988). Composite graben tectonics of Alba Patera on Mars. *Earth, Moon, and Planets*, *42*(3), 277–291. https://doi.org/10.1007/BF00058491

Richardson, J. A., Bleacher, J. E., Connor, C. B., & Glaze, L. S. (2021). Small volcanic vents of the Tharsis volcanic province, Mars. *Journal of Geophysical Research: Planets*, *126*(2), e2020JE006620. https://doi.org/10.1029/2020JE006620

Riedel, C., Michael, G. G., Orgel, C., Baum, C., van der Bogert, C. H., & Hiesinger, H. (2021). Studying the global spatial randomness of impact craters on Mercury, Venus, and the Moon with geodesic neighborhood relationships. *Journal of Geophysical Research: Planets*, *126*(3), e2020JE006693. https://doi.org/10.1029/2020JE006693

Robbins, S. J., Achille, G. D., & Hynek, B. M. (2011). The volcanic history of Mars: High-resolution crater-based studies of the calderas of 20 volcanoes. *Icarus*, *211*(2), 1179–1203. https://doi.org/10.1016/j.icarus.2010.11.012

Rodriguez, J. A. P., Zarroca, M., Linares, R., Gulick, V., Weitz, C. M., Yan, J., et al. (2016). Groundwater flow induced collapse and flooding in Noctis Labyrinthus, Mars. *Planetary and Space Science*, *124*, 1–14. https://doi.org/10.1016/j.pss.2015.12.009

Scott, E. D., Wilson, L., & Head, J. W., III. (2002). Emplacement of giant radial dikes in the northern Tharsis region of Mars. *Journal of Geophysical Research*, *107*(E4), 5019. https://doi.org/10.1029/2000JE001431

Shahrzad, S. (2023a). Ceraunius Fossae and Tractus Fossae, Mars, fault catalogue [Dataset]. *Zenodo*. https://doi.org/10.5281/zenodo.8376744

Shahrzad, S. (2023b). Ceraunius Fossae and Tractus Fossae crater catalogue [Dataset]. *Zenodo*. https://doi.org/10.5281/zenodo.8376774

Shahrzad, S. (2023c). Ceraunius Fossae and Tractus Fossae collapse features catalogue [Dataset]. *Zenodo*. https://doi.org/10.5281/zenodo.8376769

Shahrzad, S., Bramham, E. K., Thomas, M., Piazolo, S., Byrne, P. K., & Mortimer, E. (2023). Deciphering the structural history of Ulysses Fossae, Mars, using fault pattern analysis. *Journal of Geophysical Research: Planets*, *128*(5), e2022JE007633. https://doi.org/10.1029/2022JE007633

Spagnuolo, M. G., Figueredo, P. H., & Ramos, V. A. (2008). Reinterpretation of Tractus Fossae region as an asymmetric rift system on Mars. *Icarus*, *198*(2), 318–330. https://doi.org/10.1016/j.icarus.2008.08.007

Stubblefield, R. K. (2018). Extensional tectonics at Alba Mons, Mars: A case study for local versus regional stress fields [Master of Science]. North Carolina State University. http://www.lib.ncsu.edu/resolver/1840.20/36604

Tanaka, K. L. (1990). Tectonic history of the Alba Patera—Ceraunius Fossae region of Mars. In *Lunar and Planetary Science Conference Proceedings* (Vol. 20, pp. 515–523).

Tanaka, K. L., Golombek, M. P., & Banerdt, W. B. (1991). Reconciliation of stress and structural histories of the Tharsis region of Mars. *Journal of Geophysical Research*, *96*(E1), 15617–15633. https://doi.org/10.1029/91JE01194

Tanaka, K. L., Skinner, J. A., Jr., Dohm, J. M., Irwin, R. P., III., Kolb, E. J., Fortezzo, C. M., et al. (2014). *Geologic map of Mars (scientific investigations map) 3292*. U.S. Department of the Interior, U.S. Geological Survey. https://doi.org/10.3133/sim3292

van Wyk de Vries, B., & Matela, R. (1998). Styles of volcano-induced deformation: Numerical models of substratum flexure, spreading and extrusion. *Journal of Volcanology and Geothermal Research*, *81*(1), 1–18. https://doi.org/10.1016/S0377-0273(97)00076-0

Werner, S. C. (2009). The global Martian volcanic evolutionary history. *Icarus*, *201*(1), 44–68. https://doi.org/10.1016/j.icarus.2008.12.019

Werner, S. C., Ivanov, B. A., & Neukum, G. (2009). Theoretical analysis of secondary cratering on Mars and an image-based study on the Cerberus Plains. *Icarus*, *200*(2), 406–417. https://doi.org/10.1016/j.icarus.2008.10.011

Wilson, L., & Head, J. (2000). Tharsis-radial graben systems as the surface manifestation of plume-related dike intrusion complexes: Models and implications. *Journal of Geophysical Research*, *107*(E8). https://doi.org/10.1029/2001JE001593

Wilson, L., Scott, E. D., & Head, J. W., III. (2001). Evidence for episodicity in the magma supply to the large Tharsis volcanoes. *Journal of Geophysical Research*, *106*(E1), 1423–1433. https://doi.org/10.1029/2000JE001280

Wyrick, D., Ferrill, D. A., Morris, A. P., Colton, S. L., & Sims, D. W. (2004). Distribution, morphology, and origins of Martian pit crater chains. *Journal of Geophysical Research*, *109*(E6). https://doi.org/10.1029/2004JE002240